Analysis and Control Design of a Cable-Suspended Parallel Robot Under Consideration of Non-linear Effects

Redacted version. Full version available at the X-lab

Dabian Oosterloo

Master of Science Thesis

TU Delft Delft University of Technology

Delft Center for Systems and Control

MSCCONFIDENTIAL

Analysis and Control Design of a Cable-Suspended Parallel Robot Under Consideration of Non-linear Effects

Redacted version. Full version available at the X-lab

Master of Science Thesis

For the degree of Master of Science in Systems and Control at Delft University of Technology

Dabian Oosterloo

December 7, 2018

Faculty of Mechanical, Maritime and Materials Engineering (3mE) · Delft University of Technology

Laboratory

A Robotics Engineering Laboratory and R&D Accelerator

This study was conceived, designed and performed at the Delta Labs B.V. X Laboratory, hereafter called "X-Lab". *NB This is a redacted version of the thesis where confidential information has been omitted. A complete version is available at the X-lab*

TU Delft Delft University of Technology

DCSC

Abstract

The process of laying deepwater pipelines requires the constant supply of pipe segments to the pipe-laying vessel since downtime in operation is costly. A smaller vessel supplies these pipe segments, where a crane transfers them onto the pipe-laying vessel. These crane systems are required to be safe, yet efficient, even during harsh sea conditions. For this reason, a new crane has been developed by that should allow for the active compensation and tracking of vessel motions in 6 degrees-of-freedom. This potentially removes the need for humans to aid in grabbing a pipe segment. The problem is to find out how to properly control this crane for this purpose. The main goal of this thesis is therefore to *derive, identify and verify a kinematically and dynamically accurate model of the system and use it for system analysis, controller design and testing in simulation.*

From the analysis of the obtained model it is found that the system is mechanically limited to controlling only 5 degrees-of-freedom, excluding roll. It further shows that negative tension can occur during operation depending on the configuration of the crane. A controller is designed of a

that handles compensation and tracking in the controllable degrees-of-freedom.

The controlled model is subjected to two realistic trajectories that simulate the motions of the vessels under different weather circumstances. Results show that the controller performs far within its requirements for *calm weather conditions* and just outside of the requirements for *worst-case weather conditions.* Since the model has been validated to accurately represent the system, the proposed control strategy is deemed a viable candidate for solving the problem. A rearrangement in cable configuration of the crane is lastly proposed that allows for the control of roll motions.

The control of an offshore crane to compensate motions in 6 degrees-of-freedom in general is beneficial to the safety and efficiency of payload transfer during harsh sea conditions and the contents of this thesis can therefore likely be extended and applied to other applications within offshore. This motivates to verify the controller experimentally in future work.

Dabian Oosterloo CONFIDENTIAL Information. Property of X-lab M.Sc. thesis

Table of Contents

List of Figures

List of Tables

Preface

This study was conceived by Dr. Andre Schiele of the X laboratory in supplement of an ongoing collaboration between X laboratory and on their system. This study has been performed by the author at the X-lab and all information concerning its contents has been provided by Dr. Schiele in verbal and written manner during meetings with him. With this thesis, I would like to present a previously absent simulation model for the *existing* system along with a formally designed controller using the tools and knowledge that I have gathered during my master of Systems & Control at the TU Delft.

I would also like to take time here to acknowledge some people whom have helped and guided me towards the successful fruition of this thesis.

First and foremost my daily supervisor Dr. Andre Schiele who has had great interest in the topic and has been giving a helping hand throughout the entire process; especially during some of the measurements where his assistance was crucial, and in particular towards the end where his advice has helped make some difficult decisions. Besides his formal and professional guidance, I would also like to thank him for providing a fun and flexible working environment.

The study is further written under the supervision Prof. Hans Hellendoorn of the TU Delft. My gratitude goes towards him for providing me with the necessary feedback and guidance for the proper completion of this thesis on behalf of the university.

I would finally want to thank my parents, brother and sister, friends and some close fellow students. They have helped me to power through some of the difficulties that come with writing a thesis. More importantly however, they helped me get through more personal difficulties that ultimately aided in the successful completion of this thesis.

Delft, University of Technology — Dabian Oosterloo
December 7, 2018

Dabian Oosterloo CONFIDENTIAL Information. Property of X-lab M.Sc. thesis

Chapter 1

Introduction

is equipped with two that can pick up from another boat called the . The challenge when is that are constantly in motion that is induced by ocean waves. A *new* design has been developed that should allow for the automatic compensation of the motions of , as well as the tracking of motions of the such that the process for is faster and undisturbed by any unwanted, unnecessary and potentially dangerous movements. Naturally, a controller is required for these purposes. Since the operating costs for are high, limited time is available for the implementation and testing of a controller for the *actual* . For this purpose, X-laboratory has developed HIL , which can be used for system commissioning, improvement and R&D for new and better (semi-)automatic control at little cost. Despite the low costs, implementing different controllers on the test-bed is still a time-consuming process due to the complexity of the system. A model of the test-bed system is therefore also desired that allows for easy and quick examination of different controllers. *This thesis will be focusing on obtaining such a model. Furthermore, a preliminary controller will be designed to verify that the model can indeed be used for its intended purpose.* Figure 1-1 shows a block-diagram of the road map to the final goal and the *contribution* of this thesis towards achieving it.

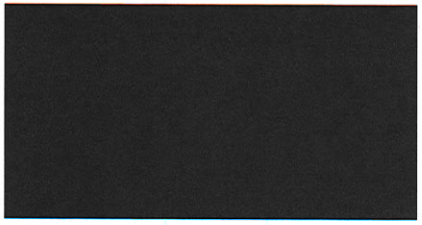

Figure 1-1: Road map towards achieving the final goal of controlling the , outlined in red. The black outlined blocks already exist. The dashed line indicates the contribution that this thesis will be making. A controller will be designed for the model, which in future work is then implemented on the test-bed and adjusted until it performs properly. It can finally be implemented on and adjusted again.

The remainder of this chapter will further elaborate on the system components that have been mentioned and provide the necessary background information for the proper understanding of the thesis in general, starting with a description of the system. Then continuing with the proper classification of such a system and a review of their state of the art. Next, a formal statement of the problems that need to be solved in this thesis and the goals that it sets to do so, follow from the shortcomings found in the literature. Finally, the scope will be defined and the approach will be outlined.

1-1 System description

A top-down description of the situation, environment and system is first given along with important terms and concepts. This section will gradually converge on the specific part of the system that will be modeled and controlled.

1-1-1

, according to . Figure 1-2 shows . The relative distance between both can be as high as 50m. Note that figure 1-2 shows the *old*, purely manually operated, . This thesis shall focus on the *new* that is still manually operated in hoisting and lowering, but can switch to an *automatic* mode for tracking.

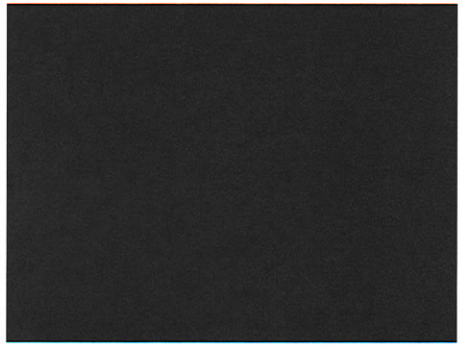

Figure 1-2: are seen in operation on the left side. The relative distance between both can be up to 50m. Courtesy of

Environment specifications The weather conditions under which operates cause it and the to exhibit motions in all six Degrees Of Freedom (DOF). They can be mathematically defined by performing a calculation based on the JONSWAP spectrum that is typical for North sea waves [1] while also taking into account the angle of attack of waves, reflection of these waves between the vessels, vessel shape as well as vessel masses. The frequency range of these ocean waves and the maximum significant wave height are given in

table 1-1. The worst-case scenario occurs when the ocean waves reach their highest point and highest frequency for an *angle of attack* of 225 degrees. Figure 1-3 depicts this situation schematically.

Max freq.	Min freq.	Significant wave height
0.33 [Hz]	0.0016 [Hz]	4.5 [m]

Table 1-1: Worst-case wave specifications for the North sea.

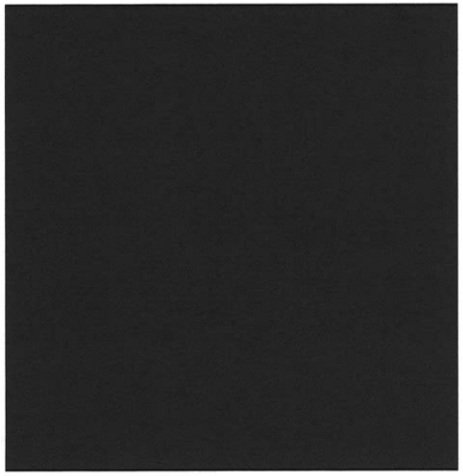

Figure 1-3: Worst-case scenario for motions where the wave frequency is 0.33Hz, significant wave height 4,5m and angle of attack 225 degrees. Note that this depict the worst-case scenario for the *real* system

1-1-2

The

They can both be seen in operation in figure 1-2. The form a sub-system which will be referred to as the system.

The system is the part of the system that allows motion compensation and tracking, shown schematically in figure 1-4. It has a mounted on the to measure the instantaneous poses of the *simultaneously*. It has

The notations used in this thesis for each of the 6 DOF in which both the can move is given in table 1-2. Note that in figure 1-4, these notations are extended with a sub-script that corresponds to the frame to which they belong, where frame Ψ_A is the frame and Ψ_B the frame.

Table 1-2: Symbol notation for each degree of freedom as used in this thesis

DOF	Surge	Sway	Heave	Roll	Pitch	Yaw
Symbol	x	y	z	ϕ	θ	ψ

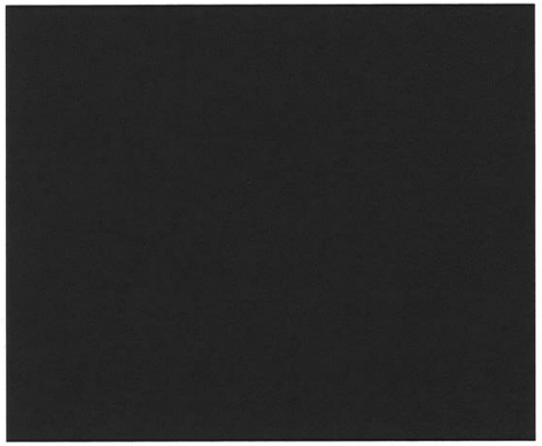

Figure 1-4: Simplified drawing of the subsystem. The movements of the in all six DOF are subscripted by their frame conventions Ψ_A and Ψ_B, respectively. A reference for name conventions is also drawn.

1-2

Figure 1-5 shows schematically the set-up for the test-bed. *All dimensions, parameters and environmental specifications are scaled with dynamic similitude by a factor of 12.* The upper will be referred to as the and its *end-effector* simulates the motions of the tip of the . The will be referred to as the and its end-effector simulates motion of the . The relative distance between both scales to about 4m. A dynamically scaled version of the system is attached to the simulator including the . is available to verify measurements. Furthermore, figure 1-3 shows the graphical interface for the directions of waves that can be selected for the simulation.

The *scaled* version of the will be the main focus of this thesis. Therefore, a short classification and review on similar systems is now provided

1-3 System Classification and Challenges

The sub-system can be classified as a *parallel mechanism*, where a number of parallel links are used to manipulate the end-effector. Perhaps the most famous example of a parallel mechanism is the *Stewart-Gough* platform [2]. A sub-class of parallel systems, called Cable-Driven Parallel Mechanism (CDPM) utilizes the basic idea of a Stewart-Gough platform but

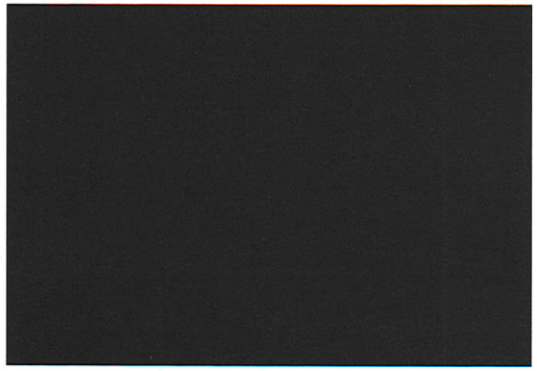

Figure 1-5: Simplified drawing of the test-bed consisting of two and an external camera system for verification (Vicon). Frames are again drawn for the . The relative distance between both can be about 4m. Another frame is drawn for the measures the difference between the motions of the

uses cables as the parallel links and winches on the actuators. In case of the sub-system, the is the end-effector and is linked together by 8 kinematics chains, being the cables. The use of 8 cables for the control of 6 DOF further makes the a *redundant* or *over-actuated* system. For the and as a consequence, the only downward acceleration is obtained by gravity. Such systems are a sub-class of CDPM commonly referred to as Cable-Suspended Parallel Mechanism (CSPM). The use of cables brings some mayor advantages such as increased workspace and higher dynamic capabilities according to Gosselin [3].

However, a significant drawback comes from the fact that **cables can only operate in tension**, i.e. they can only pull, not push. This motivates the review of similar systems and state of the art for those systems that are either related to the specific application of motion compensation/tracking in offshore systems, or to the control of CDPM/CSPM where the challenges that arise from using cables are addressed. *In other words, to find out how motion is generally compensated in offshore application and how the prevention of negative cable tensions typically dealt with.*

1-3-1 Review of State of the Art

Motion compensation in offshore applications is a widely researched field, in particular for lifting purposes one can refer to Neupert et al. [4], Kuchler et al. [5], Xiangling et al. [6]. Compensation in these cases however is only done for a single DOF, namely heave. Compensation for multiple-degrees-of-freedom is also researched by Ngo and Hong [7], [8] and Kim and Lee [9]. These studies considered systems that are
but still lack certain DOF. Furthermore, there is no mention on negative cable tension or how to prevent it, which indicates that the authors have assumed weather conditions where this does not occur. Since the worst-case scenario for is likely to induce a relative motion between that *will* cause negative tensions, the control approaches of these systems are not likely to be sufficient.

For studies that *do* address the cable tension problem and can move the end-effector in 6 DOF using parallel cable configurations, refer to Gholami et al [10], Laroche et al. [11] and Chellal et al. [12]. These systems however are as they belong to the CDPM class defined above. In other words, the cables surround the end-effector in all directions. This allows for large internal dynamics which can be used to control the tension as desired, which is generally not possible for CSPM. The same method has nevertheless been found in literature for CSPM such as Lamaury et al. [13] and [14], but with limited effect. Other studies on CSPM systems have been found to adopt an algorithm that limits the reference when negative tensions occur, in Oh et al. [15] or methods of *virtually* removing cables in combination with force control as in Meunier et al. [16] to ensure positive tensions throughout operation. These systems, as well as most of the ones mentioned before, only assume the end-effector as moving and the frame to which the actuators are mounted as fixed.

It is apparent that all of the above mentioned studies fall short in providing a complete treatment or solution to the problem at hand, which can now properly be defined

1-4 Problem Statement

In summary, the *specific problem* is that of picking up s from the . Both the exhibit motions induced by the environment, with specific worst-case specifications for which the process of picking up s should still be possible. A Cable-Suspended Parallel Mechanism (CSPM) called the will be utilized for this purpose. It can be manually operated when hoisting and lowering and can switch to an automatic mode where it will start to track the motions of the whilst still compensating for motions of .

Therefore, the problem that arises from the specific problem and from the shortcomings in the literature, can be formulated as a *general problem*:

How to control the end-effector of a redundant CSPM system for offshore application that compensates motions and allows good position tracking for all 6 DOF, seeks to keep cable tensions positive at all times and has a moving actuator frame?

Sub-problems The sub-problems relate to the general problem defined above. They are therefore specifically problems related to control.

1. Which control structure can be used?
   (a) How to design and tune this controller?
   (b) How to ensure positive cable tensions?
   (c) How to deal with over-constrained actuation?
2. Which error margin defines good tracking?
   (a) For which conditions does the controller still yield good tracking?
   (b) How to ensure stability?

1-5 Thesis goal and Scope

The contribution of this thesis towards solving the specific problem is to *derive, identify and verify a kinematically and dynamically accurate model of the system and use it for system analysis, controller design and testing in simulation.* A list of research questions that follow from the general problem statement, sub-problems and thesis goal are now given.

Research questions the research questions relate to the thesis goal defined in this section. They are therefore specifically questions related to modeling

1. Which modelling approach balances performance and computation time?
   (a) Which dynamics need to be captured by the model?
   (b) Does the model include all the challenges of the system? (Moving WF in 6 DOF; over-actuated; occurrence of negative tension; non-linear effects)
   (c) What is the computation time of the simulation?
2. How to verify the model?
   (a) How accurate does the model need to be?
3. What are the limitations of the system?
   (a) How can the limitations be mathematically or numerically analyzed and predicted?
   (b) How do these limitations depend on the chosen cable configuration?

1-5-1 Limitations, exclusions and requirements

This section will define the constraints that are in effect on the system set-up and establish the boundaries of the research to derive the scope of the thesis.

Practical constraints No open-loop measurements that includes the
Firstly because the parallel nature of the system can easily cause instability which in turn can cause one of the cables to break, creating a dangerous environment. Secondly because the set-up is already in use and a controller is running on the system for testing during the time of executing this thesis. *Therefore, verification of the model cannot include actuator dynamics.*

Since the dynamics cannot be verified and because it would be a highly time consuming undertaking to properly identify, the actuator frictions shall be neglected throughout this thesis. However, it will be shown how to include them in the model for future inclusion. The same goes for any disturbances, e.g wind.

Scope This thesis shall limit the controller design to only one operating point at the centre of the workspace. The design of the controller then becomes trivial for the other operating points, however many are required.

Controller requirements The controller requirements are based on the environment specifications of table 1-1 and the worst-case scenario that was presented in figure 1-3. From these calculations, minimum and maximum values for each DOF of both are obtained relative to their own respective frames. These values are given in table 1-3. *Note that these values are scaled for the test-bed set-up.*

Table 1-3: worst-case motion for each DOF and frequency band, relative to their own respective frames. Note that these values are for the test-bed.

DOF	Ampl. [m/rad]	Freq. [Hz]	Ampl. [m/rad]	Freq. [Hz]
Surge	-0.0188 to 0.0188	0.21-1.16	-0.1105 to 0.1106	0.23-1.16
Sway	-0.0087 to 0.0088	0.21-1.16	-0.0863 to 0.0865	0.23-1.16
Heave	-0.0248 to 0.0247	0.22-1.16	-0.3179 to 0.3173	0.23-1.16
Roll	-0.0067 to 0.0067	0.21-1.16	-0.0270 to 0.0269	0.23-1.16
Pitch	-0.0065 to 0.0065	0.22-1.16	-0.2164 to 0.2164	0.23-1.16
Yaw	-0.0033 to 0.0033	0.22-1.16	-0.1068 to 0.1066	0.23-1.16

The bandwidth of the motion controller is therefore required to be at least $1.16 * 2\pi = 7.3$ rad/s as a frequency-domain requirement. For time-domain requirements, proper tracking is here defined by the minimal

1-6 Approach and Outline

In part I, a kinematic and dynamic model of the system is obtained by Newton-Euler and Lagrange methods where the parameters are obtained by measurement of the system, cable stiffness identification using a dedicated set-up and system identification of the entire set-up. The model will then be verified with respect to the actual system. Finally, the model is linearized for analysis and controller design purposes.

In part II, the general control strategy is first given based on knowledge gathered thus far. This gives rise to a formal description for the occurrence of negative tensions. Next, the linear model is used for the dynamic analysis of the system and the kinematic model for the kinematic analysis. The linear model further allows for the design of a motion controller and a force controller.

Part III presents the simulation results of the controller on a realistic test scenario. The final chapter of this part will then discuss the results and answer the sub-problems, research questions and problem statement. A list of recommendations is then given to further improve results. A concluding chapter follows that will list all of the conclusions that can be drawn from this thesis.

Part I

Modeling

Chapter 2

General model

It has been established that the is a parallel robot. Two types of models are required to fully describe the motion of a robot, namely a *kinematic* model and a *dynamic* model.

The kinematics of a robot is understood as all the allowed movements that the robot can adopt without regard of the forces or torques that cause it. It is solely concerned with how the robot can be described in terms of position, velocity and acceleration [17]. There are two distinct ways in which the *pose* (position and orientation) of a robot's end-effector can be described; either in Cartesian coordinates known as the Task-Space (TS), or in joint variables known as the Joint-space (JS). Kinematic modelling comes down to finding a *mapping* between these two spaces where the Inverse Kinematics (IK) is the mapping from TS to JS coordinates and the Forward Kinematics (FK) is the mapping from JS to TS coordinates.

Dynamic modelling of a robot means to obtain the *equations of motion* that govern its dynamic behavior under the influence of wrenches (forces and moments) acting on it. For robots, these are typically the forces supplied by the actuators, forces due to friction and due to interaction with the environment, i.e. disturbances. For the , the dynamic components consist of a *rigid body that is the* , the *cables* and the *actuators/winches*.

The following sections shall derive these models for the , starting with kinematic modeling. Then, a general dynamic model for the , cables and actuators/winches is derived. The specific parameters of the model are obtained by simple measurements of its geometry and by an identification of the cable stiffness and damping through experiment. The model is also verified by using a motion capture camera system on the test-bed set-up.

2-1 Kinematic Modeling

For parallel systems, kinematic modeling in practically all cases is done by vector analysis of the robot. It obtains the link/cable lengths as a function of the end-effector pose by looking at the vectors that describe the attachment point positions and the end-effector position. The frequent use of this method is apparent by looking at studies that apply it,

e.g. [10, 11, 14, 16, 18, 19]. For the general kinematic modelling used in these studies, the base frame is fixed and the cables are first considered as rigid links. Figure 2-1 shows graphically the vectors that are used for this analysis. For the gives rise to a slightly more complex model that has not been found addressed in the literature. However, the , which simplifies its influence on the system.

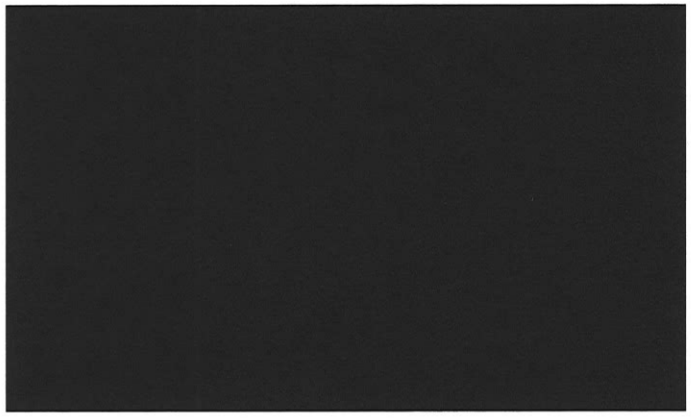

Figure 2-1: Kinematic model for the system. The red vectors indicate the vector analysis for a single cable (cable 7). The

Let the following vectors and variables be defined for the modelling of the system:

$$
\begin{aligned}
\mathbf{x}_{wf} = [\mathbf{p}_{wf}^T \quad \mathbf{o}_{wf}^T]^T &\quad \text{TS coordinates of pose with Euler angle convention where} \\
&\quad \mathbf{p}_{wf} = [x_{wf} \quad y_{wf} \quad z_{wf}]^T \text{ and } \mathbf{o}_{wf} = [\phi_{wf} \quad \theta_{wf} \quad \psi_{wf}]^T \\
\mathbf{x}_{sb} = [\mathbf{p}_{sb}^T \quad \mathbf{o}_{sb}^T]^T &\quad \text{TS coordinates of SB pose with Euler angle convention where} \\
&\quad \mathbf{p}_{sb} = [x_{sb} \quad y_{sb} \quad z_{sb}]^T \text{ and } \mathbf{o}_{sb} = [\phi_{sb} \quad \theta_{sb} \quad \psi_{sb}]^T \\
\mathbf{l} = [l_1 \quad l_2 \quad \cdots \quad l_8]^T &\quad \text{JS coordinates of cable lengths (stretched)} \\
\mathbf{l}_0 = [l_{01} \quad l_{02} \quad \cdots \quad l_{08}]^T &\quad \text{Un-stretched cable lengths} \\
\mathbf{w} = [\mathbf{f}^T \quad \mathbf{m}^T]^T &\quad \text{Vector of wrench (force and moment)} \\
\mathbf{t} = [t_1 \quad t_2 \quad \cdots \quad t_8]^T &\quad \text{Vector of cable tensions} \\
\mathbf{q} = [q_1 \quad q_2 \quad \cdots \quad q_8]^T &\quad \text{Vector of angles} \\
\boldsymbol{\tau} = [\tau_1 \quad \tau_2 \quad \cdots \quad \tau_8]^T &\quad \text{Vector of}
\end{aligned}
\tag{2-1}
$$

2-1-1 Inverse Kinematics

The vector analysis results in an expression for the cable vector as a function of the poses, expressed in the fixed reference-frame Ψ_r:

$$\begin{aligned} \mathbf{l}_i &= \mathbf{p}_{bi} - \mathbf{p}_{ai} \\ &= (\mathbf{p}_B + \mathbf{R}_B^r \mathbf{b}_i) - (\mathbf{p}_A + \mathbf{R}_A^r \mathbf{a}_i) \\ &= \mathbf{p} + \mathbf{R}_B^r \mathbf{b}_i - \mathbf{R}_A^r \mathbf{a}_i \\ \text{for} \quad i &= 1, 2, ..., 8 \end{aligned} \tag{2-2}$$

Where $\mathbf{l}_i$ is the cable vector for the i^{th} cable expressed in the reference-frame Ψ_r, $\mathbf{a}_i$ is the vector from the origin of the -frame to the i^{th} attachment point expressed in the -frame Ψ_A; $\mathbf{b}_i$ is the vector from the frame to the i^{th} attachment point of the expressed in the -frame Ψ_B; $\mathbf{p}_A$ is the vector for the translation from reference-frame to -frame expressed in frame Ψ_r; $\mathbf{p}_B$ is the vector for the translation from reference-frame to -frame expressed in frame Ψ_r; $\mathbf{R}_B^r$ is the rotation matrix of frame Ψ_B with respect to frame Ψ_r. It can be obtained in several ways by rotating along certain different axis. In most literature however, the matrix is found by rotating subsequently along the three axis of the inertial frame [14, 18, 19]. The rotation matrix can then be derived by a pre-multiplication of these three basic rotation matrices as:

$$\begin{aligned} \mathbf{R}_B^r(\phi_{sb}, \theta_{sb}, \psi_{sb}) &= \mathbf{R}_z(\psi_{sb})\mathbf{R}_y(\theta_{sb})\mathbf{R}_x(\phi_{sb}) \\ &= \begin{bmatrix} c\phi & -s\phi & 0 \\ s\phi & c\phi & 0 \\ 0 & 0 & 1 \end{bmatrix} \begin{bmatrix} c\theta & 0 & s\theta \\ 0 & 1 & 0 \\ -s\theta & 0 & c\theta \end{bmatrix} \begin{bmatrix} 1 & 0 & 0 \\ 0 & c\psi & -s\psi \\ 0 & s\psi & c\psi \end{bmatrix} \\ &= \begin{bmatrix} c\phi c\theta & c\phi s\theta s\psi - s\phi c\psi & c\phi s\theta c\psi + s\phi s\psi \\ s\phi c\theta & s\phi s\theta s\psi + c\phi c\psi & s\phi s\theta c\psi - c\phi s\psi \\ -s\theta & c\theta s\psi & c\theta c\psi \end{bmatrix} \end{aligned} \tag{2-3}$$

Where s and c represent the sine and cosine function and the subscript 'sb' has been left out for brevity; ϕ is the angle of rotation around the x-axis, θ is the angle of rotation around the y-axis and ψ is the angle of rotation around the z-axis.

$\mathbf{R}_A^r$ is the rotation matrix of frame Ψ_A with respect to frame Ψ_r. It can be obtained by another set of rotations about each axis for the -movements:

$$\mathbf{R}_A^r(\phi_{wf}, \theta_{wf}, \psi_{wf}) = \mathbf{R}_z(\psi_{wf})\mathbf{R}_y(\theta_{wf})\mathbf{R}_x(\phi_{wf}) \tag{2-4}$$

By taking the norm of (2-2), the actual length of the cables can be obtained, giving an expression for the IK:

$$\begin{aligned} l_i^2 &= \|\mathbf{l}_i\|^2 = \mathbf{l}_i^T \mathbf{l}_i \\ l_i &= \pm\sqrt{\mathbf{p}^T\mathbf{p} + \mathbf{b}_i^T\mathbf{b}_i + \mathbf{a}_i^T\mathbf{a} + 2\mathbf{p}^T\mathbf{R}_B^r\mathbf{b}_i - 2\mathbf{p}^T\mathbf{R}_A^r\mathbf{a}_i - 2\mathbf{b}_i^T\mathbf{R}_r^B\mathbf{R}_A^r\mathbf{a}_i} \\ \text{for} \quad i &= 1, 2, ..., 8 \end{aligned} \tag{2-5}$$

Hence, for a given pose of the there generally exist 2 real solutions for each cable length. However, the negative solution is not physically feasible and only the positive solution remains. When the solution is instead a complex number, the given pose of the is not reachable. This derivation is almost identical to that of a Stewart platform and is described by Tsai in [17], *with the addition here of a reference frame to include WF motion.*

2-1-2 Jacobian Analysis

The IK of (2-5) provides the mapping for the *positions* in TS coordinates to JS coordinates. To obtain the mapping between these spaces for the *velocities* of the in Cartesian coordinates (TS) and in joint coordinates (JS), i.e. change in cable length over time, the time derivative of the IK can be taken. Differentiating 2-5 with respect to time yields (from Jacobian analysis, Appendix ??):

$$\dot{\mathbf{l}} = \mathbf{J}\dot{\mathbf{x}}, \quad \text{Where} \quad \mathbf{J} = \begin{bmatrix} \mathbf{u}_1^T & (\mathbf{R}_B^r\mathbf{b}_1 \times \mathbf{u}_1)^T \\ \mathbf{u}_2^T & (\mathbf{R}_B^r\mathbf{b}_2 \times \mathbf{u}_2)^T \\ \vdots & \vdots \\ \mathbf{u}_8^T & (\mathbf{R}_B^r\mathbf{b}_8 \times \mathbf{u}_8)^T \end{bmatrix} \begin{bmatrix} \mathbf{I}_{3x3} & \mathbf{0}_{3x3} \\ \mathbf{0}_{3x3} & \mathbf{J}_\omega \end{bmatrix} \tag{2-6}$$

In which $\dot{\mathbf{l}} = [\dot{l}_1 \quad \dot{l}_2 \quad \cdots \dot{l}_8]^T$ is the vector of JS cable length changes, $\dot{\mathbf{x}} = [\mathbf{v} \quad \dot{\mathbf{o}}]^T$ the vector of TS velocities and $\mathbf{u}_i = \frac{\mathbf{l}_i}{\|\mathbf{l}_i\|}$ the unit vector for each cable. The matrix $\mathbf{J}_\omega$ is the mapping from Euler angle derivatives $\dot{\mathbf{o}}$ to angular velocities $\boldsymbol{\omega}$, as seen in Lamaury et al. [14]:

$$\boldsymbol{\omega} = \mathbf{J}_\omega\dot{\mathbf{o}}, \quad \text{Where} \quad \mathbf{J}_\omega = \begin{bmatrix} 1 & 0 & -\sin\theta \\ 0 & \cos\phi & \cos\theta\sin\phi \\ 0 & -\sin\phi & \cos\theta\cos\phi \end{bmatrix} \tag{2-7}$$

2-2 Dynamic Modelling

Dynamic modelling of the end-effector for these type of systems is most often done by either Newton-Euler, like in [10], [11], [18] and [14] or by applying the Lagrange equations, like in [19] and [8] Dynamic modeling is here proposed to be be done in a three-fold manner using these methods where the are first considered separately and are then combined.

2-2-1

The dynamics can be derived by means of the Lagrange equations, given by:

$$\frac{d}{dt}\left(\frac{\partial T}{\partial \dot{\mathbf{x}}}\right) - \frac{\partial T}{\partial \mathbf{x}} + \frac{\partial V}{\partial \mathbf{x}} = Q^{ncons} \tag{2-8}$$

Where T and V are the kinetic and potential energy of the system, respectively. The vector $\mathbf{x}$ contains the coordinates that describe the pose of the end-effector in task-space and Q^{ncons}

are the non-conservative forces of the system (wrench due to cable forces, disturbances). With kinetic energy:

$$T = \frac{1}{2} m \mathbf{v}^T \mathbf{v} + \frac{1}{2} \dot{\mathbf{o}}^T \mathbf{R}_B^r \mathbf{I}_B (\mathbf{R}_B^r)^T \dot{\mathbf{o}} \tag{2-9}$$

Where $\mathbf{v} = [\dot{x} \quad \dot{y} \quad \dot{z}]^T$ and $\dot{\mathbf{o}} = [\dot{\phi} \quad \dot{\theta} \quad \dot{\psi}]$; m is the mass of the and $\mathbf{I}_B$ is the inertia matrix for the and is transformed to the reference-frame through $\mathbf{R}_B^r$ by the *parallel axis theorem* as seen in Zi et al. [19] and Lamaury et al. [14], where

$$\mathbf{I}_B = \begin{bmatrix} \frac{1}{12} m(h_{sb}^2 + w_{sb}^2) & 0 & 0 \\ 0 & \frac{1}{12} m(h_{sb}^2 + l_{sb}^2) & 0 \\ 0 & 0 & \frac{1}{12} m(w_{sb}^2 + l_{sb}^2) \end{bmatrix} \tag{2-10}$$

From the perspective of the , the cables can be regarded as force elements, the potential energy will therefore only be dependent on gravity and is given by:

$$V = m g z_{sb} \tag{2-11}$$

where g is the acceleration due to gravity. This now allows to derive the equations of motion by filling in for T and V in (2-8) and computing each term. This results in as many equations as there are generalized coordinates that describe the dynamic behaviour of the system. This means that there are six equations of motion. An often used convention in robotics is to rewrite these equation in matrix form in the following way:

$$\mathbf{M}(\mathbf{x})\ddot{\mathbf{x}} + \mathbf{c}(\mathbf{x}, \dot{\mathbf{x}}) - \mathbf{g}(\mathbf{x}) - \mathbf{w}_D = \mathbf{w} \tag{2-12}$$

Where $\mathbf{M}$ is the positive-definite symmetric inertia matrix, $\mathbf{c}$ is the vector containing the centrifugal and Coriolis terms, $\mathbf{g}$ is the vector of gravitational force and $\mathbf{w}_D = [\mathbf{f}_D^T \quad \mathbf{m}_D^T]^T$ is the disturbance wrench vector of disturbance forces and moments acting on the . The wrench vector $\mathbf{w}$ is the vector of forces and moments acting on the due to cable forces and can be obtained through the Jacobian (from the principal of virtual work, Appendix **??**):

$$\mathbf{w} = -\mathbf{J}^T \mathbf{t} \tag{2-13}$$

The negative sign in (2-13) comes from the frame convention, which is pointing downward. In other words, positive tensions $\mathbf{t}$ should result in an upward force, corresponding to a negative value in the downward pointing frame.

2-2-2 Cable model

The cables are modelled as

11 , the cable model derives the un-stretched length from the payload position and tension by recognizing from Hooke's law that (first neglecting damping):

$$t_i = E A_{0i} \epsilon_i \tag{2-14}$$

Where t_i is the i^{th} cable tension, E is Young's modulus of the cables and A_{0i} the cross-sectional area. The elongation ϵ_i is given by:

$$\epsilon_i = \frac{l_i - l_{0i}}{l_{0i}} \tag{2-15}$$

It is assumed that the cable is wound without slipping. During the winding process, a rotation of angle $\mathrm{d}q_i$ winds a portion of the stretched cable $\mathrm{d}l_i$, even if the cable length remains constant:

$$\mathrm{d}l_i = -r_i \mathrm{d}q_i \tag{2-16}$$

Where r_i is the radius of the i^{th} winch. The corresponding decrease of the un-stretched length can be established by rearranging (2-15) as:

$$\mathrm{d}l_{0i} = \frac{\mathrm{d}l_i}{(1 + \epsilon_i)} \tag{2-17}$$

Now substituting (2-16) into (2-17) and dividing both sides by $\mathrm{d}t$ yields the differential equation:

$$\begin{aligned} \dot{l}_{0i} &= -\frac{r_i}{(1 + \epsilon_i)} \dot{q}_i \\ &= -\frac{r_i l_{0i}}{l_i} \dot{q}_i \end{aligned} \tag{2-18}$$

Next, with damping included, the tension in the cables is assumed to be the summed result of its stiffness and damping components, seen in literature by Garcia-Fernandez et al. in [20], i.e:

$$\begin{aligned} t_i &= k_i(l_i - l_{0i}) + b_i(\dot{l}_i - \dot{l}_{0i}) \\ &= k_i(l_i - l_{0i}) + b_i(\dot{l}_i + \frac{r_i l_{0i}}{l_i} \dot{q}_i) \end{aligned} \tag{2-19}$$

This gives the cable model for each cable that relates motor angular velocity $\dot{q}_i$ to cable tension t_i. The equation can be written in matrix form for all eight cables:

$$\mathbf{t} = \mathbf{K}(\mathbf{l} - \mathbf{l}_0) + \mathbf{B}(\dot{\mathbf{l}} + \mathbf{L}^{-1} \mathbf{N}_d \mathbf{R}_w \mathbf{L}_0 \dot{\mathbf{q}}) \tag{2-20}$$

Where $\mathbf{l}_0 = [l_{01} \quad l_{02} \quad \cdots \quad l_{08}]^T$ and $\dot{\mathbf{l}}_0$ its time derivative. The matrix $\mathbf{L} = \mathrm{diag}(\mathbf{l})$ is a diagonal matrix with the cable lengths $l_1, \cdots, l_8$ on its diagonal. The same holds for the matrix $\mathbf{L}_0 = \mathrm{diag}(\mathbf{l})$). The diagonal matrix $\mathbf{R}_w$ contains the winch radii and $\mathbf{N}_d = \mathrm{diag}([n \quad n \quad 1 \quad 1 \quad 1 \quad 1 \quad 1 \quad 1])$ is a diagonal matrix where the first 2 entries are the *gear-ratio* $n = 10$ for the hoist cable actuators which use gearboxes. The next section will further elaborate on this point. The stiffness matrix $\mathbf{K}$ and damping matrix $\mathbf{B}$ are to be determined experimentally, which is done in section 3.

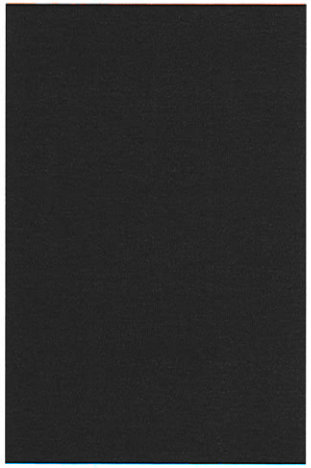

Figure 2-2: model for a single cable. Consisting of a . The latter two cause a torque on the .

2-2-3

For the dynamics, consider a single cable as shown in Figure 2-2 with the . The are fixed to the and thus only their inertia needs to be modeled. An external which results in an angular acceleration $\ddot{q}$. The is being counteracted by the torque that results from the cable tension $\tau_{ci} = r_i l_{ci}$, where t_i is given in (2-19), this yields:

(2-21)

Where $I_{w,i}$ is the combined inertia of the respectively.

The hoist cables need to be able to carry not only the SB but also the payload. This requires the which is achieved by adding a . This changes the dynamics for these in the following way (see appendix ?? for derivation):

(2-22)

Where I_{gb} is the inertia of the
The full equation can be written in matrix form for all eight winches:

(2-23)

Where $\mathbf{I}$ is the diagonal matrix containing all the motor and gearbox inertia's, $\mathbf{q}$ is the vector of motor angles and its derivatives their angular velocity and acceleration. The matrix $\mathbf{R}_w$ is the diagonal matrix of radii of the winches. The tension $\mathbf{t}$ is a function of the stiffness and damping of the cables and the matrices $\mathbf{F}_v$ and $\mathbf{F}_s$ are diagonal matrices containing the dry and viscous friction terms of each actuator.

2-3 Final non-linear model

The full robot dynamics are given by substituting (2-13) and (2-23) into (2-12) and (2-6) to obtain:

$$\mathbf{M}(\mathbf{x})\ddot{\mathbf{x}} + \mathbf{c}(\mathbf{x}, \dot{\mathbf{x}}) - \mathbf{g}(\mathbf{x}) - \mathbf{w}_D = \mathbf{J}^T \mathbf{R}_w^{-1}(\mathbf{I}\ddot{\mathbf{q}} + \mathbf{F}_v\dot{\mathbf{q}} + \mathbf{F}_s \text{sgn}(\dot{\mathbf{q}}) - \mathbf{N}_d\boldsymbol{\tau}) \tag{2-24}$$

The model of 2-24 is rather sophisticated. For the remainder of this thesis, the model shall be simplified somewhat by neglecting friction and not including disturbance forces. Therefore, 2-24 simplifies to (also leaving out the dependencies):

$$\mathbf{M}\ddot{\mathbf{x}} + \mathbf{c} - \mathbf{g} = \mathbf{J}^T \mathbf{R}_w^{-1}(\mathbf{I}\ddot{\mathbf{q}} - \mathbf{N}_d\boldsymbol{\tau}) \tag{2-25}$$

This finally allows to bring the kinematic model and all dynamic models of the , winches and cables together. Figure 2-3 shows a block diagram of the final model with motor torques $\boldsymbol{\tau}$ and motion $\mathbf{x}_{WF}$ as *inputs* and actuator angle and angular velocity $\mathbf{q}$,$\dot{\mathbf{q}}$, position and velocity $\mathbf{x}_{SB}$, $\dot{\mathbf{x}}_{SB}$ and cable tensions as the *outputs*.

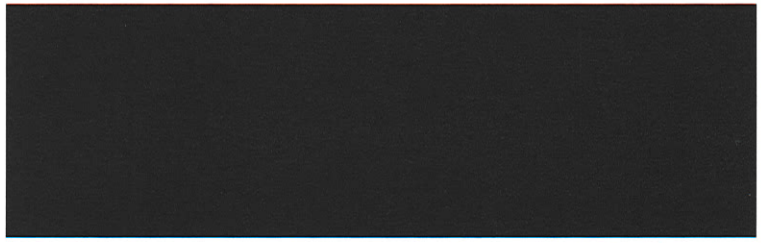

Figure 2-3: Block diagram of the model with input

The three system blocks are denoted by and their input-output relations are given by their dynamics as derived in this chapter:

$$\begin{aligned} &\text{SB:} \quad \ddot{\mathbf{x}}_{SB} = \mathbf{M}^{-1}(\mathbf{w} - \mathbf{c} + \mathbf{g}) \qquad \text{Cables:} \quad \mathbf{t} = \mathbf{K}(\mathbf{l} - \mathbf{l}_0) + \mathbf{B}(\dot{\mathbf{l}} - \dot{\mathbf{l}_0}) \\ &\qquad \mathbf{w} = -\mathbf{J}^T\mathbf{t} \qquad\qquad\qquad\qquad\quad \dot{\mathbf{l}} = \mathbf{J}\dot{\mathbf{x}} \\ &\text{Act:} \quad \ddot{\mathbf{q}} = \mathbf{I}^{-1}(\mathbf{N}_d\boldsymbol{\tau} - \mathbf{R}_w\mathbf{t}) \qquad\qquad \dot{\mathbf{l}_0} = -\mathbf{L}^{-1}\mathbf{N}_d\mathbf{R}_w\mathbf{L}_0\dot{\mathbf{q}} \end{aligned} \tag{2-26}$$

2-4 State-space model and Linearization

The non-linear model that has now been derived will be used for simulation purposes to test the performance of a controller. For model analysis and for the controller design however, it is useful to also derive a linear model as there exist many tools for these purposes for linear models that do not exist for non-linear models. *The limitation is that a linear model is only an approximation that is valid around a certain operating point of the system.* First, the model shall be written in state-space form. Let $\mathbf{x}$ denote the state vector.

$$\mathbf{x} = [\underbrace{x \quad y \quad z \quad \phi \quad \theta \quad \psi}_{\mathbf{x}_1} \quad \underbrace{\dot{x} \quad \dot{y} \quad \dot{z} \quad \dot{\phi} \quad \dot{\theta} \quad \dot{\psi}}_{\mathbf{x}_2} \quad \underbrace{q_1 \cdots q_8}_{\mathbf{x}_3} \quad \underbrace{\dot{q}_1 \cdots \dot{q}_8}_{\mathbf{x}_4} \quad \underbrace{l_{01} \cdots l_{08}}_{\mathbf{x}_5}]^T \tag{2-27}$$

Hence, the non-linear model of (2-26) is of order 36. The inputs $\mathbf{u}$ are the de-noted by $\boldsymbol{\tau} = [\tau_1 \cdots \tau_8]^T$, the pose given by $\mathbf{x}_{WF} = [x_{WF} \quad y_{WF} \quad z_{WF} \quad \phi_{WF} \quad \theta_{WF} \quad \psi_{WF}]^T$ and the gravitational constant g:

$$\mathbf{u} = [\boldsymbol{\tau} \quad \mathbf{x}_{WF} \quad g]^T \tag{2-28}$$

Finally, the outputs of the model are the measured positions $\mathbf{x}_1$ and velocities $\mathbf{x}_2$ and the cable tensions $\mathbf{t} = [t_1 \cdots t_8]^T$, measured by .

$$y = [\mathbf{x}_1 \quad \mathbf{x}_2 \quad \mathbf{t}]^T \tag{2-29}$$

In state-space form, the equations of motion of (2-26) can be written as:

$$\underbrace{\begin{bmatrix} \dot{\mathbf{x}}_1 \\ \dot{\mathbf{x}}_2 \\ \dot{\mathbf{x}}_3 \\ \dot{\mathbf{x}}_4 \\ \dot{\mathbf{x}}_5 \end{bmatrix}}_{\dot{\mathbf{x}}} = \underbrace{\begin{bmatrix} \mathbf{x}_2 \\ \mathbf{M}^{-1}(\mathbf{x}_1)(-\mathbf{J}^T(\mathbf{x}_1, \mathbf{x}_{WF})\mathbf{t}(\mathbf{x}_1, \mathbf{x}_5, \mathbf{x}_{WF}) - \mathbf{c}(\mathbf{x}_1, \mathbf{x}_2) + \mathbf{g}(\mathbf{x}_1)) \\ \mathbf{x}_4 \\ \mathbf{I}^{-1}(\mathbf{N}_d\boldsymbol{\tau} - \mathbf{R}_w\mathbf{t}(\mathbf{x}_1, \mathbf{x}_5, \mathbf{x}_{WF}) \\ -\mathbf{L}^{-1}(\mathbf{x}_1, \mathbf{x}_{WF})\mathbf{N}_d\mathbf{R}_w\mathbf{x}_5\mathbf{x}_4 \end{bmatrix}}_{f(\mathbf{x},\mathbf{u},\boldsymbol{\Theta})}, \quad \mathbf{y} = \underbrace{\begin{bmatrix} \mathbf{x}_1 \\ \mathbf{x}_2 \\ \mathbf{t} \end{bmatrix}}_{g(\mathbf{x},\mathbf{u},\boldsymbol{\Theta})} \tag{2-30}$$

Where $\boldsymbol{\Theta}$ is the vector of robot parameters. This model can be linearized around equilibrium point k by taking the derivatives of (2-30) such that:

$$\dot{\mathbf{x}} = \mathbf{A}_k\mathbf{x} + \mathbf{B}_k\mathbf{u}, \quad \mathbf{y} = \mathbf{C}_k\mathbf{x} + \mathbf{D}_k\mathbf{u} \tag{2-31}$$

Where $\mathbf{A}_k \in \mathbb{R}^{36\times36}$, $\mathbf{B}_k \in \mathbb{R}^{36\times15}$, $\mathbf{C}_k \in \mathbb{R}^{20\times36}$ and $\mathbf{D}_k \in \mathbb{R}^{20\times15}$. As seen in Laroche et al. [11], they are computed by:

$$\begin{aligned} \mathbf{A}_k &= \frac{\delta f}{\delta \mathbf{x}}(\mathbf{x}_k, [\mathbf{0}_{14\times1} \quad g]^T, \boldsymbol{\Theta}) \qquad \mathbf{B}_k = \frac{\delta f}{\delta \mathbf{u}}(\mathbf{x}_k, [\mathbf{0}_{14\times1} \quad g]^T, \boldsymbol{\Theta}) \\ \mathbf{C}_k &= \frac{\delta g}{\delta \mathbf{x}}(\mathbf{x}_k, [\mathbf{0}_{14\times1} \quad g]^T, \boldsymbol{\Theta}) \qquad \mathbf{D}_k = \frac{\delta g}{\delta \mathbf{u}}(\mathbf{x}_k, [\mathbf{0}_{14\times1} \quad g]^T, \boldsymbol{\Theta}) \end{aligned} \tag{2-32}$$

Note that the linearization is performed for input pose equal to zero and that the robot parameters are independent of the operating point $\mathbf{x}_k = [\mathbf{x}_{1,eq} \quad \mathbf{x}_{2,eq} \quad \mathbf{x}_{3,eq} \quad \mathbf{x}_{4,eq} \quad \mathbf{x}_{5,eq}]^T$. Therefore, the system can be linearized around any arbitrary operating point defined by $f(\mathbf{x}, \mathbf{u}, \boldsymbol{\Theta}) = 0$ and solving for states $\mathbf{x}$:

$$\begin{aligned} \mathbf{x}_{1,eq} &= [0 \quad 0 \quad z_{eq} \quad 0 \quad 0 \quad 0]^T & \mathbf{x}_{4,eq} &= [0 \quad 0 \quad 0 \quad 0 \quad 0 \quad 0 \quad 0 \quad 0]^T \\ \mathbf{x}_{2,eq} &= [0 \quad 0 \quad 0 \quad 0 \quad 0 \quad 0]^T & \mathbf{x}_{5,eq} &= \mathbf{L}_{eq} - \mathbf{K}_{eq}^{-1}\mathbf{t}_{eq} \\ \mathbf{x}_{3,eq} &= -\left(\mathbf{N}_d\mathbf{R}_w\right)^{-1}\mathbf{x}_{5,eq} \end{aligned} \tag{2-33}$$

Where $\mathbf{t}_{eq}$ and $\mathbf{L}_{eq}$ are the cable tensions and lengths at the operating point obtained from (2-13) and (2-5) respectively and substituted into (2-18) and rearranged to an expression for the un-stretched cable lengths $\mathbf{x}_{5,eq}$.

The stiffness matrix $\mathbf{K}_{eq}$ is obtained by evaluating the stiffness model (3-7) at the cable lengths and tensions of the equilibrium point. *The stiffness model is yet to be determined, but its evaluated value around an operating point will simply result in a diagonal matrix of stiffness values that are valid for that specific point.* Linearizing around the operating point will yield the linear model of the that is valid for configurations close to this operating point, which can be used for the design of the controller.

For the remainder of this thesis, the linear model that will be used is obtained for the operating point $\boldsymbol{x}_{1,eq} = [0 \quad 0 \quad 2m \quad 0 \quad 0 \quad 0]^T$ *as this is the physical centre of the system.*

Chapter 3

Identification

For the derived model of (2-26) to represent the test-bed, the specific parameters of the system will need to be determined. Some of these can be measured, such as the geometric parameters; others are to be found by system identification, such as the cable stiffness and damping. This chapter shows how these parameters have been obtained and in particular how the cable dynamics have been identified separately.

3-1 Geometrical and measured parameters for kinematic model

The geometry of the system is defined by the sizes of the and attachment points on both. In the test-bed set-up, these parameters are gathered by simple measurement, design or manufacturer data and are given in Appendix ?? in the form of a schematic drawing containing all dimensions and a table with their values.

In figure 2-1, are not drawn. *Rather, only the points where the cables exit the are shown as the attachment points.* In reality, the cables are first guided by pulleys to deal with the angles of the cables during operation, resulting in *additional* cable length. Furthermore, there is a small region from the attachment point where the are mounted that is considered rigid and thus is to be *subtracted* from the cable length that defines its stiffness. This means that the actual cable lengths for each cable are offset by a fixed value, i.e. for the hoist cables $l_{HO,i} = l_i + \underbrace{(l_{ho} - l_{lc,ho})}_{l_{di}}$. The same holds for the surge and sway cables. Where l_{ho} is the cable length between winch and pulley and $l_{lc,ho}$ is the load cell region. The values for l_{di} are shown in table 3-1.

Table 3-1: Cable offset

The full kinematic model, using the geometric data, can now be derived for the and it is shown drawn in Figure 3-1 using the earlier derived kinematic relations for the . In the figure, the cables are drawn using the kinematics by taking the unit vector $\mathbf{u}_i$ for each cable and multiplying it by its length l_i, obtained from (2-5), i.e. $\mathbf{l}_i = l_i \mathbf{u}_i$

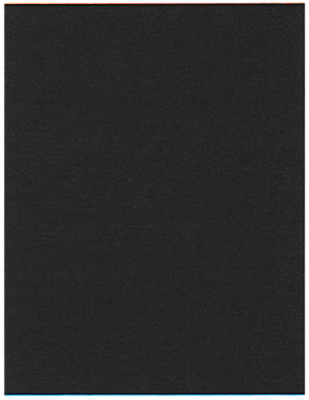

Figure 3-1: Kinematic model of the real system with all geometric parameters taken from the test-bed set-up. Note that the hoist cables (blue) are drawn thicker that the surge (red) and sway (green) cables. The surge cables in turn are drawn a bit thicker than the sway cables, which are the thinnest

3-2 Cable identification for dynamic model

Since the cables in the system most prominently define the dynamic behaviour of the system, an identification of their dynamic properties is performed with the goal of obtaining an accurate model to capture these dynamics.

3-2-1 Cable stiffness identification method

The measurement set-up for the experiment is shown in figure 3-2 on the left. It consists of a single motor with a gearbox to achieve up to 100N of tension in the cable that is wound on a winch that is equipped with a torque sensor on one end. The motor itself is equipped with an encoder for the angular position and velocity. The other end of the cable is attached to a force sensor. A schematic representation of the set-up is shown in figure 3-2 on the right. This model will later be used for the optimization of the dynamic parameters.

For this set-up the gravity acting on the cable is neglected and the model of the cable and the actuator are derived from (2-18) and (2-21) respectively:

$$\begin{bmatrix} -\frac{rl_0}{l}\dot{q} \\ I_w\ddot{q} + rt \end{bmatrix} = \begin{bmatrix} \dot{l}_0 \\ \tau \end{bmatrix} \tag{3-1}$$

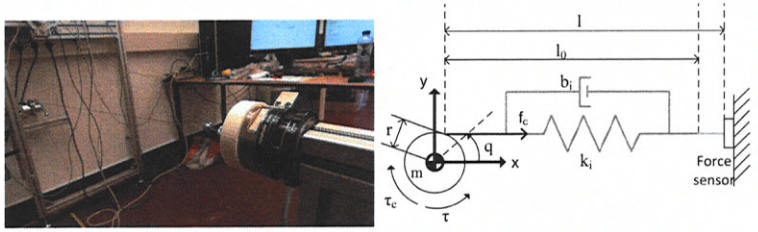

Figure 3-2: Left: Actual set-up for cable identification consisting of a position controller motor, the cable to be identified and a force/torque sensor. **Right:** Model of set-up used for optimization of parameters.

Where I_w is the equivalent inertia of the motor, gearbox and winch combined, r is the radius of the winch and t is the tension of the cable. The input for this set-up is a motor torque τ and the outputs are the cable tension t, the motor angle q and angular velocity $\dot{q}$. The tension t of (3-1) is equal to the magnitude of the force shown in figure 3-2 and is measured by the force sensor *directly*. Therefore, the motor inertia and torque are not required to be known for the identification of the stiffness and damping. As shown in (2-19), the tension of the cable is determined by its stiffness k and a damping factor b:

$$t = k(l - l_0) + b(\dot{l} - \dot{l}_0) \tag{3-2}$$

Where $\dot{l} = 0$ since the cable is fixed. First, the stiffness of the cables will be identified. *To isolate only the contribution of stiffness to the tension, all dynamics should be suppressed such that $\dot{l}_0$ is negligibly small.* In this case, according to (3-1), also $\dot{q}$ is negligible and therefore $\ddot{q}$ as well. This simplifies (3-1) to:

$$\begin{aligned} \tau &= rt \\ &= rk(l - l_0) \end{aligned} \tag{3-3}$$

Suppressing the dynamics is achieved by defining a proper input signal for this experiment, i.e. one with little to no dynamic behaviour. A low frequency trapezoidal signal is one such signal and will be used for the cable stiffness identification. The system of figure 3-2 will be position controlled since the encoder has a high resolution and can therefore accurately be controlled. This means that the motor will move a certain angle in one direction, stretch the cable and then move back in the other direction where the cable is slowly un-stretched again. Naturally, the motor needs to be limited in its movement as to not stretch the cables past their breaking force. The cables used in the

. Different diameters are used for hoist, surge and sway cables based on their required tensions to hold. Table 3-2 shows the parameters of the cables that are used, including their diameters and breaking force according to the manufacturer:

Table 3-2: Maximum allowed forces of the cables with a Safety Factor (SF)

The breaking forces given by the manufacturer are maximum values. The cables will not be equally strong at every point and especially at those points where they are mounted or deformed can they break at lower forces. For this reason, a safety factor is often applied to the maximum allowed forces in cable systems. A common value for this factor for running wires is 5, of which the results are also shown in table 3-2. These values are further rounded such that they balance safety and performance and are also given in table 3-2, along with the actual safety factors. Note that the actual safety factors are still higher than 3, which is generally found to be a minimum for cable applications. The hoist cable forces are limited even further since higher forces are not required for the purposes of the system.

The motor angular position and the cable force are measured during the experiment. This data is first filtered using a butterworth filter with a cut-off frequency at 2Hz. The filtered data is then used to calculate the stiffness at each time-interval (1000Hz sample rate) by taking the ratio of the change in force with respect to the change in cable stretch, where the latter is obtained from the motor angular position times the radius of the winch, i.e. $l_0 = rq$ where $r = 0.025$m, in the following way:

$$k(j) = \frac{t(j+1) - t(j)}{l_0(j+1) - l_0(j)} \tag{3-4}$$

Where t is the cable tension measured by the force sensor, l_0 is the un-stretched length of the cable measured by the encoder and j is the time-step index.

3-2-2 Stiffness identification results

The responses shown in the figures of 3-3 are the mean result of 4 trapezoidal cycles of stretching and un-stretching the cables when applying (3-4) to the measurement data. A small hysteresis effect can be observed in the responses between the cable being stretched (up) and un-stretched (down). This effect is neglected for the purposes of this study and the mean response between the two is assumed for both directions.

The figures clearly show that indeed the cable stiffness is inversely proportional to its length as given by Hooke's law (2-14), i.e $k(l_0) = \frac{EA_0}{l_0}$. The Young's modulus E that is given by the manufacturer however (table **??**), is only that of the material. It does not take into account the construction of the cable and for this reason it can be seen that there is be a significant deviation from this value. Hence, instead of EA_0, a parameter a will be used.

From the measurements shown in the figures above, and from other literature such as Miermeister et al. [21], it is also found that the stiffness of the cable changes as the cable is stretched. From observation there are a variety of potential functions that could fit the relation between tension and stiffness. Six of these functions have been applied to the data

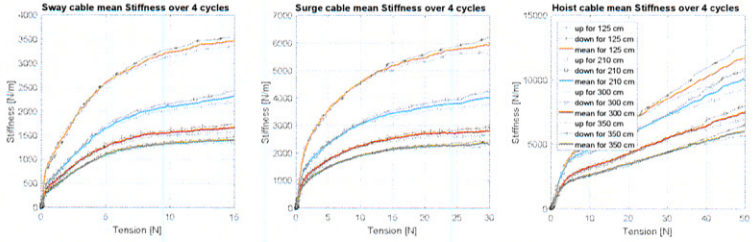

Figure 3-3: Sway, surge and hoist cable stiffness plotted for four different lengths as a function of tension. A distinction is made between stretching the cable (up) and un-stretching the cable (down). For further analysis however, the mean value is taken and assumed for both up and down, also shown in the figure

in order to determine which fits best. The process of determining this function is given in Appendix 3-6 and it is found that the data adheres best to an exponential function of the form:

$$k(t) = be^{ct} + de^{et} \tag{3-5}$$

Where t is the cable tension and b, c, d and e are scalars. Note however, that for higher forces, the dependency of the stiffness on the cable tension is of a more linear nature, this is especially apparent for the hoist cables. For this reason a final parameter f is introduced as an exponent to the length l_0 that counters the exponential behaviour of (3-5) for higher tensions. *The goal now is to obtain a two-dimensional function that depends on both the cable length and cable tension for the stiffness.* Combining Hooke's law and (3-5) with the added parameter f yields such a two-dimensional function:

$$k(l_0, t) = \frac{a}{(l_0)^f}(be^{ct} + de^{et}) \tag{3-6}$$

The measurements further show that the stiffness is zero when the tension is zero. This is equivalent to stating that $b = -d$ in (3-6). Filling in this constraint and simplifying, rearranging and renaming terms, (3-6) becomes:

$$k(l_0, t) = \frac{a}{(l_0)^b}(e^{ct} - e^{dt}) \tag{3-7}$$

It remains to determine the values for a, b, c and d that provide the best fit for this function with respect to the measurements. This is done by minimizing the following cost function.

$$\begin{aligned} &\min_{a,b,c,d} \|\mathbf{K}_m - \hat{\mathbf{K}}\| \\ &\text{with} \quad \hat{\mathbf{K}} = \frac{a}{(\mathbf{l_0})^b}(e^{c\mathbf{t}} - e^{d\mathbf{t}}) \end{aligned} \tag{3-8}$$

Where the matrix $\hat{\mathbf{K}}$ is the estimate for the stiffness for each combination of length and tension that have been measured and the matrix $\mathbf{K}_m$ contains the actual measured stiffness at these points. A minimization is done of the Euclidean norm of the difference between these two matrices by using the matlab function *fmincon*. The initial values were taken approximately until proper results emerged. The following values were found after the optimization was performed.

Table 3-3: Cable stiffness model parameters for each cable

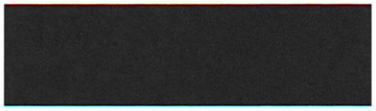

Figure 3-4 shows the resulting surface plots for each cable using the stiffness model of (3-6) with the parameters found in table 3-5. The measurement data is also included in the plot for reference.

Figure 3-5 gives a better view of this plot for the fit between each measured length and the model. Furthermore, table 3-4 gives the Variance Accounted For (VAF) values that correspond to the fit between the identified stiffness function and the measured stiffness over the specified tension ranges. The VAF can be derived as a measure of accuracy of the model as compared to the actual measurements. The VAF score is obtained by:

$$VAF = 100\left(1 - \frac{\text{var}(\mathbf{y} - \hat{\mathbf{y}})}{\text{var}(\mathbf{y})}\right) \tag{3-9}$$

Where $\mathbf{y}$ is the vector of measured values of the signal and $\hat{\mathbf{y}}$ the vector of estimated or modeled values of the signal. The VAF gives a value between 0 and 100 % which indicates how much the estimated signal corresponds to the actual signal, where 100% is an exact overlapping between the two signals.

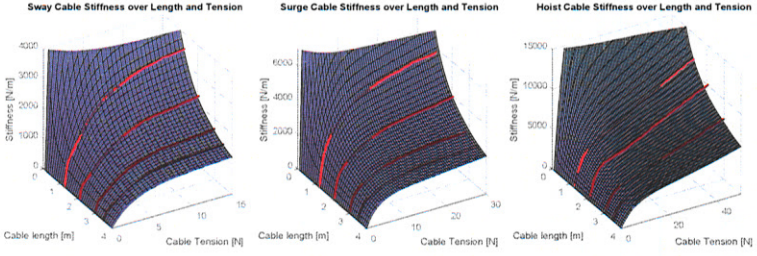

Figure 3-4: Surface plots of the sway, surge and hoist cable stiffness as a function of their length and tension. The measurement data is included in the figures, shown by the red lines.

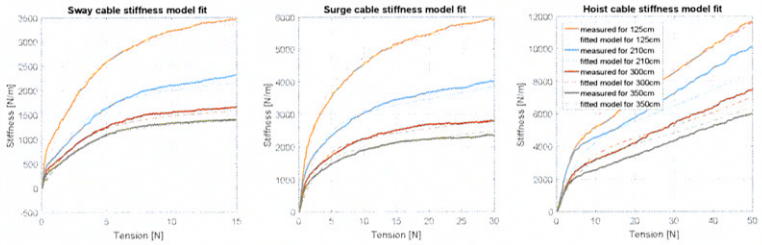

Figure 3-5: Measured stiffness and the model fit at each length for each cable. Note that the stiffness model is optimized for the specific tension range defined for each cable

Table 3-4: VAF values for the stiffness model fit with respect to the actual measured stiffness at each length

VAF (%)	125 [cm]	210 [cm]	300 [cm]	350 [cm]
Hoist	98.39	95.425	97.248	97.526
Surge	98.28	97.713	97.865	97.636
Sway	98.83	97.75	99.18	99.22

Figures 3-3, 3-4 and 3-5 further only show the cable stiffness functions up to their defined maximum values and in fact, the identified stiffness function of (3-7) is only optimized for these tension ranges. For higher tensions, the function starts to no longer captures the cable stiffness accurately because the stiffness starts behaving linearly, i.e. at higher tensions the stiffness remains constant. This can be observed in the figures by the asymptotic behaviour of the measured stiffness. This is further explained by the manufacturer in the technical specification document where two types of elongation are distinguished: constructional elongation and material elongation [22]. The cables first exhibit constructional elongation where the wires and strands move closer to each other. When the cables are further tensioned and the wires and strands are in their optimal positions, the cable themselves elongate based on the material they are made of. The constructional elongation is different for each cable and non-linear over the elongation while the material elongation is equal and almost linear for each cable (*at a specific length*). The identified stiffness functions capture the constructional elongation and the asymptotes that can be observed is where the material elongation starts. From here, the stiffness remains constant until the cable breaks.

The model of (3-7) therefore needs to be expanded to include this behaviour such that when the tension does exceed its limits it will still accurately be described by the model. This is done by finding the stiffness values for each cable for these linear sections of the cable. In fact, since all cables are made of the same material and constructed in the same way, the Young's modulus E can be identified and applied such that the final stiffness model is:

$$\begin{cases} k(l_0,t) = \frac{a}{(l_0)^b}(e^{ct} - e^{dt}) & \text{for} \quad k < \frac{EA_0}{l_0} \\ \text{else} \quad k(l_0) = \frac{EA_0}{l_0} \end{cases} \tag{3-10}$$

The value of the Young's modulus E is obtained by looking at the asympotes of the sway and surge cables in particular and applying Hooke's law. The hoist cables are much thicker and can be stretched further before reaching their asymptotes and can therefore not be used. Note that the stiffness values at the asymptotes, given in table 3-5, are an approximation.

Table 3-5: Approximated cable stiffness and corresponding Young's modulus for sway and surge cables at the asymptotes, for each measured length

By taking the mean of all the values found for the Young's modulus E in table 3-5, it is found that $E = 87215 \frac{N}{mm^2}$. Note that this is a different value than given in table **??**. The value found here is obtained from measurement and will therefore be deemed more accurate. Thus, the final stiffness model is that of (3-10) where the parameters for each cable are given in tables **??** and 3-3 and the Young's modulus is obtained from table 3-5

3-2-3 Cable damping identification method

The identification of the damping term of each cable requires measurements of the dynamic behaviour since damping acts on the velocity of the cable lengths. The input signal will therefore be a multi-sine current to the motor with frequencies up to 10Hz that will result in a tension in the cable. With the stiffness now known, the damping can be identified by optimization, using the tension model of (3-11) where b is the unknown parameter of the damping ratio. Note that the cable still needs to always be in tension for the model to be valid and that the multi-sine signal is therefore applied with a torque offset t_0. This torque offset results in a tension offset that will also be fitted and is included in (3-11).

$$t = k(l - l_0) - b\frac{rl_0\dot{q}}{l} + t_0 \tag{3-11}$$

The matlab function *lsqnonlin* is used to obtain the damping ratio and the tension offset by using the actual velocity data measured by the encoder as an input to the model and changing these parameters to fit the data as well as possible. The objective function for this optimization is given in (3-12) and is done for all three cables and for each of the four cable lengths for which the stiffness has also been identified.

$$\min_{b,t_0} \|\mathbf{t}_m - \hat{\mathbf{t}}\| \tag{3-12}$$

Where $\mathbf{t}_m$ is the measured cable tension and $\hat{\mathbf{t}}$ the estimate from the model. Figure 3-6 shows the model that is used for this optimization process.

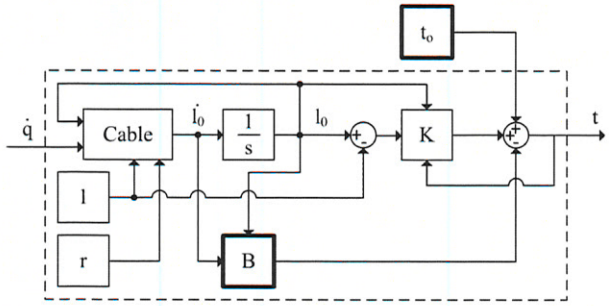

Figure 3-6: Block diagram of the model used for damping identification. Both the damping and the tension offset are identified, shown in bold outlines, by minimizing the norm of the difference between the measured tension and modeled tension

3-2-4 Damping identification results

Figure (3-7) shows the plot of the measured and optimized damping values for each length along with a linear functions that is fitted on the data by means of *least squares*. The three linear functions of the cable damping are given in (3-13). Note that no dependency on tension is included for the damping

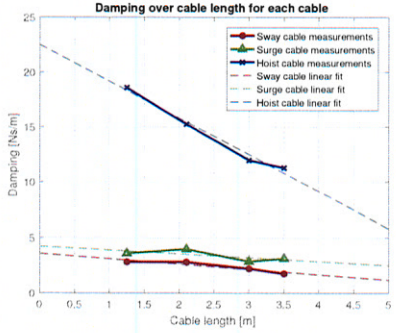

Figure 3-7: Damping values obtained from measurement and fitted to a cable tension model for each cable at four different lengths. A linear function is fitted for each cable using linear least-squares.

$$
\begin{aligned}
b_{ho}(l_0) &= 22.5 - 3.44 l_0 \\
b_{su}(l_0) &= 4.217 - 0.345 l_0 \\
b_{sw}(l_0) &= 3.55 - 0.47 l_0
\end{aligned}
\tag{3-13}
$$

Chapter 4

Verification

This chapter serves to verify that the model and parameters that have been derived and identified in the previous two chapters, correspond well to the test-bed set-up. Two measurements will be be performed. First, the cable model will be verified separately. Then, the full system is verified.

4-1 Cable model verification

The goal of the separate verification of the cable model is to ensure the validity of the cable model, which is the most important aspect of the entire model since it dictates most of the dynamics of the system.

4-1-1 Cable verification method

A final measurement on the same dedicated cable set-up from figure 3-2 is done for each cable at a different length of 180cm. The actual measured tension is then compared to the tension obtained from the model. Again, for the measurement, a multi-sine signal is used of frequencies up to 10Hz for 200 seconds. The tension offset (see figure 3-6) is assumed to be the first value of the measured tension.

4-1-2 Cable verification results

Figure 4-2 shows the measured tensions and modelled tension for each cable. For the modelled tension, the functions for the stiffness and damping that have been identified are evaluated at this length and the same multi-sine input is used.

The plots clearly show that the model fits the data well. It can be observed however that for all cables, but especially the hoist cable, the model falls somewhat short for the lower tension range. This can be explained by a variety of reasons, namely the stiffness model

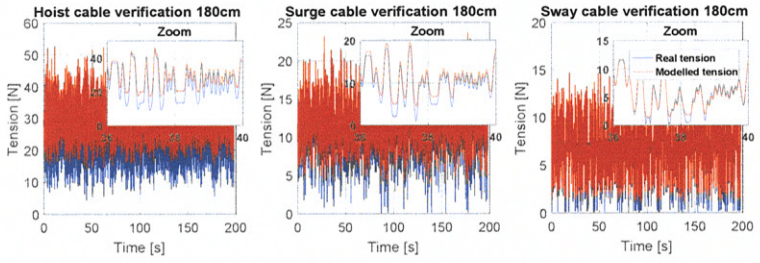

Figure 4-1: Verification of the cable model for the identified stiffness and damping functions. Each plot shows the actual tension and modelled tension for the same applied input of motor angular velocities.

not being completely accurate at this lower tension range; the hysteresis effect that is more significant for shorter cable lengths; the force offset could be slightly different or the winch radius deviates a little because of the way the cables are mounted, or a combination of these reasons. Nevertheless, the model accurately represents the real data, as is evident when the VAF is computed between each signal for each cable, given in table 4-1. *It should be noted however that there could be systematic errors in the measurement since the same set-up is used for the identification as for the verification.*

Table 4-1: Variance Accounted For (VAF) between measured output (cable tension) and modelled output for each cable at 180cm cable length

Cable	Hoist	Surge	Sway
VAF	93.987%	98.4936%	98.5434%

4-2 System model verification

It is finally left to verify the full model. The goal of this verification is again to ensure validity of the model. The entire model is verified apart from the actuators. First, the method of verification is outlined and then the results are given. Based on the results, a final adjustment to the damping parameters is done as it was found to deviate from its identified value.

4-2-1 System verification method

In the schematic drawing of the test-bed set-up in figure 1-5 it was already mentioned that an external camera system is available for measurements, called is a motion capture system that can track objects in 3D space with a maximum frame-rate of 2kHz by detecting markers that are attached to the object by using a multitude of cameras. Here, six cameras with a 5 megapixel resolution have been used to track both the at a frame rate of 100Hz such that their coupled behaviour can be identified.

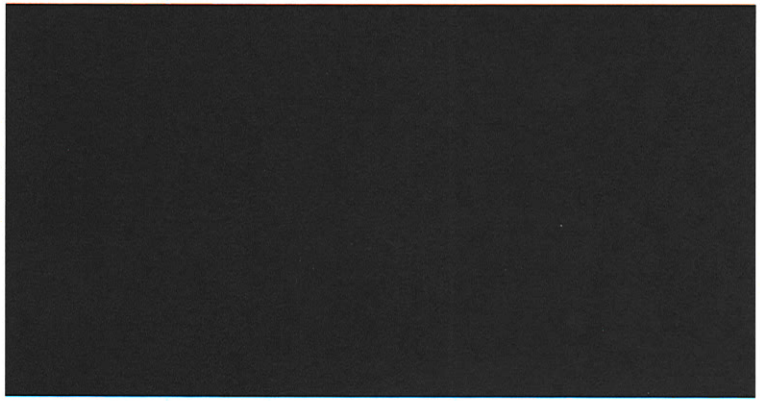

Figure 4-2: Set-up for verification measurements using . Two cameras can be seen in the picture on the left of the set-up (out of a total of six). The robots are shown on the right with the system suspended to the simulator.

The model takes two inputs as seen in figure 2-3, . The measurement will only be done for motion of the as an input. The actuator speed is zero. This means that the verification does not include as they are not moving. Furthermore, the movement is limited to moving either in sway or in the surge where the latter is actually slightly circular such that there is a coupled movement between sway and surge and will therefore be used for the verification shown here. The measurements are carried out at three different lengths of the

4-2-2 System verification results

Figure 4-3 shows the responses of the translational movement of both the measurement and the model using the same input of all three lengths. The rotations are more difficult to verify since the input does not excite these DOF as much, any error between these signals can be due to numerical issues or small non-linearities that are not captured by the model. For this reason and for brevity, the rotations are not shown in figure 4-3, but can be seen in Appendix ?? along with an elaboration on the necessary transformations between frames that were required to compare the data with the model.

Note in figure 4-3 that the identified damping of the cables from section 3-2-3 does not yield the results from measurements that are observed. The most likely reason for this is that the cable identification has only taken into account the damping in the direction along the cables, i.e. in the direction of heave of the . The measurements here are of movements in the surge and sway direction, presumably exciting the other modes of the cable that are in the orthogonal direction, for which other damping ratios apply. Damping in these directions

however is not straightforward. It will depend on the configuration of the , meaning it also depends on the cable tensions, and possibly on the velocity of the .

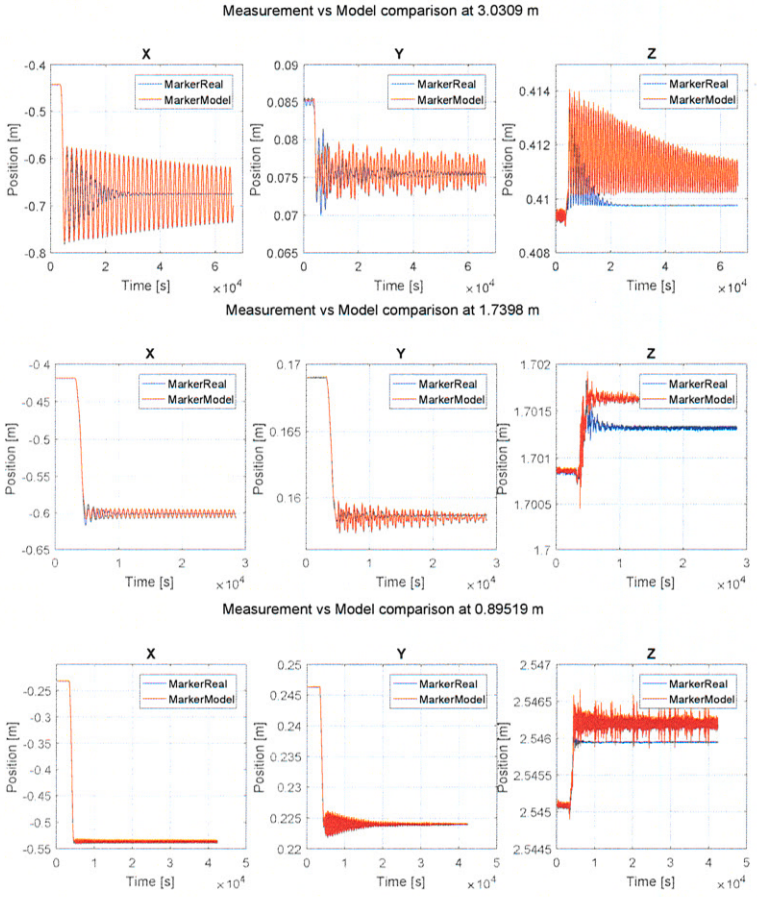

Figure 4-3: Comparison between measured and modeled data for in the negative surge direction. VAF scores are ($VAF_x = 35.55$, $VAF_y = 38.4$ and $VAF_z = 0$), ($VAF_x = 99.38$, $VAF_y = 98.78$ and $VAF_z = 55.9$) and ($VAF_x = 99.924$, $VAF_y = 99.4$ and $VAF_z = 83.412$) respectively

More important is the stiffness of the system, which dictates the resonance frequency of the . From figure 4-3 it is clear that the model does capture this well for the translations.

The damping is finally adjusted to better fit the data by manually increasing it by a certain factor for all cables. No optimization is carried out because the actual damping in any case is expected to be more complicated, but is of no significant importance for the remainder of the thesis. It only matters that there is at least some damping in the model for simulation purposes. The controller design does not heavily depend on it and it is assumed that with a correcting factor of 6, the damping of the system is sufficiently captured. Figure 4-4 shows finally the measurement data and the modeled data for the same input with the adjusted damping for all three lengths in only the direction of surge for brevity (plots for all 6 DOF are found in Appendix ??). It can further be observed that the VAF scores have significantly increased for each DOF at all lengths, which are given in the figure caption for all translations.

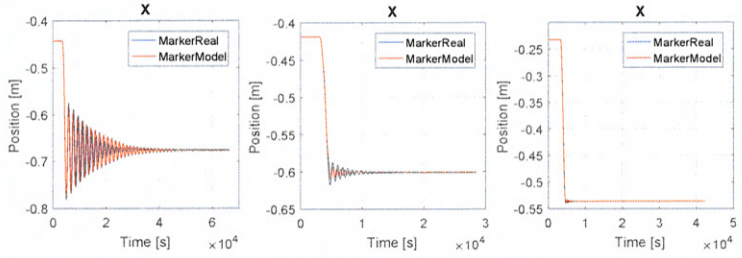

Figure 4-4: Comparison between measured and modeled data with adjusted damping. Only the surge direction is shown for brevity.
VAF scores for *all* translations are ($VAF_x = 91.41$, $VAF_y = 70.4$ and $VAF_z = 65.5$), ($VAF_x = 99.82$, $VAF_y = 99.78$ and $VAF_z = 83.82$) and ($VAF_x = 99.988$, $VAF_y = 99.55$ and $VAF_z = 95.2$) respectively

Since the in this experiment moved in the surge direction, the VAF scores for x are most important as this DOF is the one that is mostly excited. The VAF scores here are well above 90% at each length. In the sway and heave direction however, there are some VAF scores that are relatively low, mostly in the heave direction. Since this DOF is almost not excited, even small non-linearities in the system that are not included in the model can cause different behaviour on the millimeter level of motion. The sway direction is excited a bit more, and this is immediately noticeable in the VAF scores (and figures in Appendix ??)

Part II

Model Analysis & Controller Design

Chapter 5

Control strategy

Having now obtained and verified the model, a general control structure can be devised.

MC

FC

TD

16 The general control strategy that includes these controllers is given in figure 5-1.

Figure 5-1: High-level block diagram of the

MC MC

TD

FC

5-1 Tension solutions

The proposed control structure of figure 5-1 requires the transformation of desired wrench to desired cable tensions. In the figure this is denoted by the Tension Distribution block. From (2-13), a relation between wrench and cable tensions is already derived. For the controller the cable tensions are needed while the desired wrench is obtained from the MC. In other words, this relation needs to be inverted. Since the Jacobian is not a square matrix however, it is not directly invertible as this would require to find a unique solution to an over-determined system. One remedy for this problem is to find the minimum norm (Euclidean) solution, which is known as the *pseudo-inverse*. Thus by taking the pseudo-inverse of the transposed Jacobian, the cable tensions can be obtained by the ***pseudo-inverse tension solution***:

$$\mathbf{t}_{des} = -\left(\mathbf{J}^T\right)^{\dagger} \mathbf{w}_{des} \tag{5-1}$$

Where the super-script † represents the pseudo-inverse. Since the system of (2-13) is over-determined, the *right* pseudo-inverse should be taken provided that $\mathbf{J}^T$ is full rank [23].

$$\left(\mathbf{J}^T\right)^{\dagger} = \mathbf{J}^T(\mathbf{J}\mathbf{J}^T)^{-1} \tag{5-2}$$

To check whether the Jacobian is indeed full rank, a configuration of the is filled into the analytically derived Jacobian of (2-6) along with the identified parameters of the system. The centre configuration for the will be used for this computation, i.e. $\mathbf{x}_{sb,eq} = [0 \quad 0 \quad 2m \quad 0 \quad 0 \quad 0]^T$. The coordinates will all be zero. This yields a numerical Jacobian for this specific configuration:

It is immediately clear that the second and fourth column of $\mathbf{J}^T$ are linearly dependent on one another. In other words, the Jacobian $\mathbf{J}^T$ is *not* full rank but has a rank of 5. This means that only 5 DOF can be controlled. Moreover, since 8 cables are used for the control of these 5 DOF, a minimum of only 5 cables are required to fully constrain the movement of these 5

DOF (gravity acts as the sixth cable to satisfy $m = n + 1$ with m the amount of cables and n the DOF, from Berti et al. [24]).

Taking the pseudo-inverse for a rank deficient matrix requires a different approach than the one given in (5-2). The pseudo-inverse in such a case is best computed using the Singular Value Decomposition (SVD), according to Skogestad in [23]. Furthermore, in (??), the second column corresponds to the sway motion of the and the fourth column to the roll motion. This suggests that the two DOF are coupled and that one or the other is not controllable. To further analyze this behaviour, again the SVD can be used. The next chapter will therefore provide an in-depth analysis of the model using the SVD where the concept will be further explained.

Before that however, the tension solution will first be further dissected in terms of its limitations. The reason is that, as stated, the pseudo-inverse tension solution is not the only solution to this problem and it disregards the constraint of positive tensions. In other words, the minimum Euclidean norm solution of the tension might include negative values for the entries of $\mathbf{t}_{des}$ for certain configurations of the . In such a case, when this relation is used to obtain the desired tension for the , it will attempt to apply negative tensions to the system if no preventive measures are implemented. To better understand this, the causes for negative tensions are identified.

5-1-1 Causes for negative tensions

For this section, all modes of operation of the system will be discussed individually. In each of these modes, slightly different rules apply and thus negative tensions occur for several reasons. The conditions for all modes are first given; then an explanation of when negative tensions arise.

Mode 1 (Zero actuator angular velocity, i.e. $\dot{\mathbf{q}} = 0$ and zero velocity, i.e. $\dot{\mathbf{x}} = 0$)

In this mode both the are not moving and as a result, only gravity acts as an external force. The tension solution to compensate for gravity is obtained by taking as the desired wrench the opposite value of the gravity vector, i.e. $\mathbf{w}_{des} = -\mathbf{g}$, Where $\mathbf{g} = [0 \quad 0 \quad mg \quad 0 \quad 0 \quad 0]^T$. Substituting into (5-1), this becomes:

$$\mathbf{t}_{des} = \left(\mathbf{J}^T\right)^{\dagger} \mathbf{g} \tag{5-4}$$

Which will yield negative tensions for certain configurations of the . It is yet to determine which configurations these are.

Mode 2 (Non-zero actuator angular velocity, i.e. $\dot{\mathbf{q}} \neq 0$ and zero velocity, i.e. $\dot{\mathbf{x}} = 0$)

This is a mode where the actuators are moving, but the is not. It can occur since there are multiple solutions to the tension distribution for any configuration of the . The space in which the cable tensions can change such that they do not affect the pose is referred to as the *null-space* of the transposed Jacobian and shall be denoted by $\mathbf{N} = \text{kernel}(\mathbf{J}^T)$, where $\mathbf{N}$ is an 8x3 matrix. As seen in Laroche et al. [11], Lamaury et al. [14] and Khosravi et al. [25], by adding a specific term which lives in $\mathbf{N}$ to the tension solution of (5-1), the actuators can move while the does not (so only gravity is acting as an external force). This yields:

$$\mathbf{t}_{des} = \left(\mathbf{J}^T\right)^{\dagger} \mathbf{g} + \mathbf{N}\boldsymbol{\lambda} \tag{5-5}$$

Where $\boldsymbol{\lambda}$ is a 3x1 vector which scales $\mathbf{N}$. To see that the pose is not affected, $\mathbf{t}_{des}$ can be substituted back into (2-13) such that the resulting wrench on the is written as:

$$\begin{aligned} \mathbf{w}_{des} &= -\mathbf{J}^T \left(\left(\mathbf{J}^T\right)^{\dagger} \mathbf{g} + \mathbf{N}\boldsymbol{\lambda} \right) \\ \mathbf{w}_{des} &= -\mathbf{g} \end{aligned} \tag{5-6}$$

Where, by expanding the equation, the second term cancels out since $\mathbf{N}$ lives in the null-space of the transposed Jacobian, and the first term again leaves only $\mathbf{g}$ due to the Jacobian multiplied by its (pseudo-)inverse being the identity matrix. To visualize this effect, figure 5-2 shows a side-by-side comparison of the system in the configuration $\mathbf{x} = [0 \quad 0 \quad 2\text{m} \quad 0 \quad 0 \quad 0]^T$ where two different tension distributions result in the same pose of the .

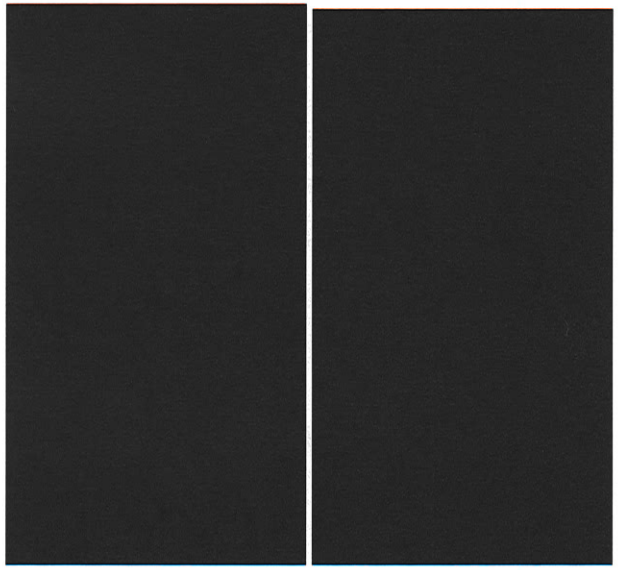

Figure 5-2: Different cable tension distribution for the same configuration. The tension in each cable is shown by the black lines where an upward line means positive tension. **Left:** Tensions resulting from (5-4). **Right:** Tensions resulting from (5-5), with an arbitrarily chosen $\boldsymbol{\lambda} = [6 \quad 0 \quad 2]^T$.

In this case, negative tensions can result when $\boldsymbol{\lambda}$ is poorly chosen, on top of certain configurations. *Note that in fact the addition of the term $\mathbf{N}\boldsymbol{\lambda}$ is not limited to this mode; it can also be applied in the first mode and in the last mode where both the actuators and are moving.*

Further note that zero velocity ($\dot{\mathbf{x}} = 0$) is with respect to the reference frame Ψ_r. This means that also when the is moving, this case holds. As a consequence, this case is not only valid for movements in the null-space, but is a common mode of operation. It will actually become clear that it is just a special case of the last mode (for non-zero actuator angular velocity and non-zero velocity). Therefore, it needs no special attention in terms of operation, but serves well as an introduction to the concept of the null-space

Mode 3 (Zero actuator angular velocity, i.e. $\dot{\mathbf{q}} = 0$ and non-zero velocity, i.e. $\dot{\mathbf{x}} \neq 0$)

This is a special mode where now the actuators are locked, but the is moving. This mode can occur when the system is in motion and the actuators suddenly stop. Clearly, this is a mode that needs to be prevented at all times and it only occurs when there is something wrong with the actuators. Such a mode falls outside the scope of this thesis and shall be assumed not to occur from this point forward.

Mode 4 (Non-zero actuator angular velocity, i.e. $\dot{\mathbf{q}} \neq 0$ and non-zero velocity, i.e. $\dot{\mathbf{x}} \neq 0$)

This is the most common mode for this system as both the actuators and the will move during operation. In this mode, gravity is no longer the only force acting on the will start playing a role. Although, as has been mentioned, mode 2 is also included in this mode and as such it *could* happen that gravity *is* the only external force acting on the for some period of time during operation. The cable tensions can be obtained by again rewriting 2-13 and the null-space term can immediately be added to obtain a ***general tension solution*** that reads:

$$\mathbf{t}_{des} = \mathbf{N}\boldsymbol{\lambda} - \left(\mathbf{J}^T\right)^{\dagger} \mathbf{w}_{des} \tag{5-7}$$

In this case, not only can the configuration cause negative tension but also the acceleration and velocity at that instantaneous pose according to (2-25). In fact, for certain accelerations and velocities it could easily happen that a pose of the that would otherwise result in negative tension according to (5-4), now results in positive tensions. Conversely, negative tension can arise at positions which would be positive if the was not moving. For example, if the in figure 5-2 would accelerate downwards with an acceleration greater than g, (5-7) will result in negative tensions. To summarize, negative tensions occur when:

- The are in poses that results in (5-4) giving negative tensions as the desired tensions for the force controller when there is no movement.
- The moves such that (5-7) results in negative tensions as the desired tensions for the force controller. Note that these movements are relative to the reference frame.
- The vector $\boldsymbol{\lambda}$ is chosen such that (5-7) results in negative tensions as the desired tensions for the .

Chapter 6

Model analysis

For the analysis of the model, the linear model of (2-31) is used. First, a dynamic model analysis is performed since this can provide insight into the rank deficiency of the Jacobian that was observed in (??). A key concept for this analysis is the *Singular Value Decomposition*, or SVD, that was briefly mentioned in the previous chapter. Additionally, because the system, and therefore model, is a Multiple Input Multiple Output (MIMO) system, it is crucial to understand how the inputs are related to the outputs. For the design of the controller, an analysis needs to be performed that can shows the coupling between inputs and outputs and the overall controllability. From Skogestad in [23], two such methods for analysis are presented, the SVD and the Relative Gain Array (RGA) The SVD and RGA can be used to quantify the degree of directionality and the level of (two-way) interactions in MIMO systems.

Secondly, a kinematic model analysis is performed that provides further information on issues like singularities, where control over one or more DOF is lost either due to a specific configuration or negative cable tensions, and the pseudo-inverse solution limitations. Furthermore, a workspace of the is derived.

6-1 Dynamic model analysis

The linear model of (2-31) has three inputs, namely and the gravitational constant as shown in (2-28). The pose and the gravitational constant however, are not control inputs but can rather be seen as disturbances. Therefore, for the model analysis the input can be selected to only consist of the . The outputs of the model are the positions and velocities and cable tensions as shown in (2-29). With the proposed cascaded control structure of figure 5-1, both outputs are separately used for a different controller. Therefore, two sub-systems can be defined: The tension sub-system and the motion sub-system. For the tension sub-system, the cable tensions are selected as the output whilst for the motion sub-system, the positions and velocities are selected. These sub-systems will be analyzed separately.

6-1-1 Motion sub-system

From the point of view of the MC, the input to the system is the wrench $\mathbf{w}$ and the outputs are the position and velocity $\mathbf{x}_{SB}$ and $\dot{\mathbf{x}}_{SB}$. Since the linear model of (2-32) is defined for actuator torques $\boldsymbol{\tau}$ as the inputs, a conversion from torques to wrench is required. To simplify this conversion, it is first assumed that the cables are rigid, i.e. a wrench on the is directly related to a tension distribution in the cable through the Jacobian according to 2-13. Furthermore, the cable tensions are assumed to be directly proportional to the through the winch radii including gear-ratio. The conversion is then obtained by:

$$\boldsymbol{\tau} = -\mathbf{N}_d^{-1}\mathbf{R}_w \left(\mathbf{J}^T\right)^\dagger \mathbf{w} \tag{6-1}$$

In state-space this corresponds to applying the same conversion to the $\mathbf{B}$ and $\mathbf{D}$ matrices where the input to the new linear system is then $\mathbf{w}$. Since the linear model of (2-32) already outputs the position and velocity, the model that is used to obtain the transfer function between $\mathbf{w}$ and $\mathbf{x}_{SB}$ is given by:

$$\begin{aligned} \mathbf{A}_m &= \mathbf{A}_k & \mathbf{B}_m &= -\mathbf{B}_k(:, 1:8)\mathbf{N}_d^{-1}\mathbf{R}_w \left(\mathbf{J}_k^T\right)^\dagger \\ \mathbf{C}_m &= \mathbf{C}_k(1:6, :) & \mathbf{D}_m &= -\mathbf{D}_k(1:6, 1:8)\mathbf{N}_d^{-1}\mathbf{R}_w \left(\mathbf{J}_k^T\right)^\dagger \end{aligned} \tag{6-2}$$

Such that the motion sub-system can be written as:

$$\dot{\mathbf{x}} = \mathbf{A}_m\mathbf{x} + \mathbf{B}_m\mathbf{w}, \quad \mathbf{x}_{SB} = \mathbf{C}_m\mathbf{x} + \mathbf{D}_m\mathbf{w} \tag{6-3}$$

Where $\mathbf{A}_m \in \mathbb{R}^{36\times36}$, $\mathbf{B}_m \in \mathbb{R}^{36\times8}$, $\mathbf{C}_m \in \mathbb{R}^{6\times36}$ and $\mathbf{D}_m \in \mathbb{R}^{6\times8}$. Refer to Appendix ?? for further details on obtaining these matrices. Note that the subscript k still denotes an operating point around which the model is linearized and that the Jacobian depends on it as well. Further note that the model inputs are only the (converted to wrench) since these are the only inputs that can be controlled and that the output is only the pose since the velocity can be obtained by differentiation in the controller. This model can now be used for analysis.

Singular Value Decomposition The main difference between a Single Input Single Output (SISO) system and a MIMO system according to Skogestad [23] is the fact that the latter exhibits *directionality* in its inputs and outputs since they are vectors instead of scalars. The SVD is a tool that is able to quantify this directionality. The SVD states that for a matrix $\mathbf{G} \in \mathbb{R}^{m\times n}$, there exists orthonormal matrices $\mathbf{U} \in \mathbb{R}^{m\times m}$ and $\mathbf{V} \in \mathbb{R}^{n\times n}$ such that the matrix $\mathbf{G}$ can be decomposed as $\mathbf{G} = \mathbf{U}\boldsymbol{\Sigma}\mathbf{V}^T$ where $\boldsymbol{\Sigma}$ is a diagonal matrix with *singular values* on the diagonal in descending order, $\mathbf{U}$ is a unitary matrix of *output singular vectors* and $\mathbf{V}$ is a unitary matrix of *input singular vectors*. A formal definition of the SVD can be found in Skogestad [23]. Naturally, the SVD is frequency dependent. For a quick analysis of the system, the SVD is computed for low frequencies (steady-state gain). The system gain $\mathbf{G}$

is obtained from (6-3) at a frequency of $\omega = 0.1$ rad/s *since the system contains integrators and the actual steady-state gain is infinity.* The following matrices are obtained:

[redacted]

Note that the values are rounded and that the actual values do give a unit norm for the columns of $\mathbf{U}$ and $\mathbf{V}$. The singular values represent the gain of the system that corresponds to the input and output directions given by $\mathbf{V}$ and $\mathbf{U}$ respectively. From the fact that there is a singular value of zero, it is immediately clear that the corresponding direction cannot be controlled. The input direction is obtained from $\mathbf{V}$ and the direction whose gain is zero is highlighted. The same applies for the output direction. The highlighted input direction shows an almost pure moment on roll (the fourth entry being 1). This suggests that any input in this direction is not visible at the output. Conversely, the largest singular value corresponds to an input force in sway that translates to mostly roll movement and a little movement in sway itself. In other words, the system is not capable of directly controlling its roll motion, but the roll is excited when a force is given in sway. *This means that when sway is to be controlled, a rolling motion of the will inevitably occur that cannot be controlled without also affecting the sway motion.*

Another quantitative measure that can be derived from the SVD is a *condition number* as the ratio between the highest singular value and the lowest. For this computation, the second lowest singular value is taken since the lowest is not of interest anymore when the control of the corresponding DOF is removed. Thus the condition number is obtained by $\gamma = \frac{\bar{\sigma}}{\underline{\sigma}} = \frac{1719}{11} = 156$. According to Skogestad, a condition number higher than 10 may indicate control problems and therefore the system is said to be *ill-conditioned.* Luckily, the stability problems related to an ill-conditioned system arise more from small minimum singular values than from large maximum singular values. This does however definitively mean that roll cannot be controlled since the system will quickly lose stability if it is.

Lastly, the singular values for a range of frequencies can be plotted, as shown in figure 6-1. *A singular value plot shows the maximum gain of the system outputs at a frequency range for all linear combinations of the inputs.* The figure shows clearly how one output is not amplified at all, whatever input is given. This output has now been determined to be the roll of the . All other directions show a similar behaviour for their singular values. The system exhibits flexible modes at frequencies between 20 and 100 rad/s, although highly damped. It behaves like a double integrator for low frequencies and a triple integrator for high frequencies.

Relative Gain Array The RGA, usually depicted by matrix $\Lambda \in \mathbb{R}^{i \times j}$, is a matrix that contains elements λ_{ij} where each element denotes the ratio of 'gain between input j and output i when all other *inputs* are kept constant' and 'gain between input j and output i when all other *outputs* are kept constant', according to Skogestad [23]. It can be computed by the element-by-element multiplication (Hadamard or Schur-product) between the system gain matrix $\mathbf{G}$ and its transposed (pseudo-)inverse at a specific frequency. The RGA is a measure of how much the inputs and outputs are coupled or, otherwise put, it shows which

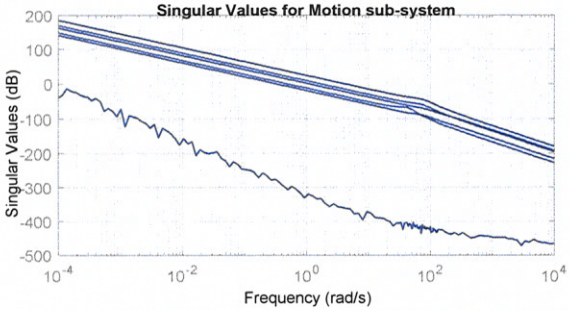

Figure 6-1: Singular values for the model of (6-2) showing the maximum gain of the system of each output for all linear combinations of the input in a certain frequency range. The bottom plot corresponds to the singular value of zero in (??) which is known to be the roll of the .

inputs should ideally be paired with which output. The closer to 1 an entry is, the more influence the input has to the corresponding output and hence should be paired with. For its computation, a frequency of $\omega = 0.1$ rad/s will again be used.

[redacted]

The values closest to 1 are given in bold. It can be observed that there are 4 input/output pairs that are perfectly decoupled, namely those for surge, sway, pitch and yaw (x, z, θ, ψ). The input moment on the roll can again be seen to not be coupled to any output and the sway input force is strongly coupled with the roll output motion. Note that these numbers are relative to each other and that the large effect on the roll for input forces on sway does not mean that there is no effect on the sway motion. *Hence, if the control for roll is neglected, the system can be said to be perfectly decoupled and controllers can be designed based on the same methods as for SISO systems.* This means that 5 controllers need to be designed that determine the desired wrench $\mathbf{w}_{des}$ based on the error signal. This is done in section 7-1.

6-1-2 Tension sub-system

From the point of view of the FC, the input to the system are the actuator torques $\boldsymbol{\tau}$ and the output the cable tensions $\mathbf{t}$. The linear model of (2-32) is already defined for actuator torques as the inputs, therefore no conversion is required. The state-space model for this sub-system is obtained by:

$$\begin{aligned} \mathbf{A}_t &= \mathbf{A}_k & \mathbf{B}_t &= \mathbf{B}_k(:, 1:8) \\ \mathbf{C}_t &= \mathbf{C}_k(13:20, :) & \mathbf{D}_t &= \mathbf{D}_k(13:20, 1:8) \end{aligned} \tag{6-6}$$

Such that the force sub-system can be written as:

$$\dot{\mathbf{x}} = \mathbf{A}_t\mathbf{x} + \mathbf{B}_t\boldsymbol{\tau}, \quad \mathbf{t} = \mathbf{C}_t\mathbf{x} + \mathbf{D}_t\boldsymbol{\tau} \tag{6-7}$$

Where $\mathbf{A}_t \in \mathbb{R}^{36\times36}$, $\mathbf{B}_t \in \mathbb{R}^{36\times8}$, $\mathbf{C}_t \in \mathbb{R}^{6\times36}$ and $\mathbf{D}_t \in \mathbb{R}^{6\times8}$. Refer to Appendix ?? for further details on obtaining these matrices.

Singular Value Decomposition In the same way as for the motion sub-system, the SVD for the tension sub-system is computed for a frequency of $\omega = 0.1$ rad/s. The matrices are given in (??).

The $\mathbf{U}$ and $\mathbf{V}$ matrices show that in fact the input and output directions are similar to a large extent. Which means that for a certain input direction, a similar output direction is excited. This already indicates that the inputs and outputs are at least to some extent decoupled, even though it is not perfect as the motion was for the input wrench. Furthermore, the singular values show that the condition number for this sub-system is $\gamma = \frac{228}{32.2} = 7.08$, which means that the system is *well-conditioned* in this case, and therefore controllable for each output. Figure 6-2 shows also the singular values for each frequency for the tension sub-system.

The system has flexible modes between 40 and 90 rad/s. It behaves as a static gain up to these frequencies and as a single integrator at higher frequencies. Note that because the system behaves like a static gain for the lower to mid-range frequencies, the corresponding $\mathbf{U}$ and $\mathbf{V}$ matrices do not change either for these frequencies.

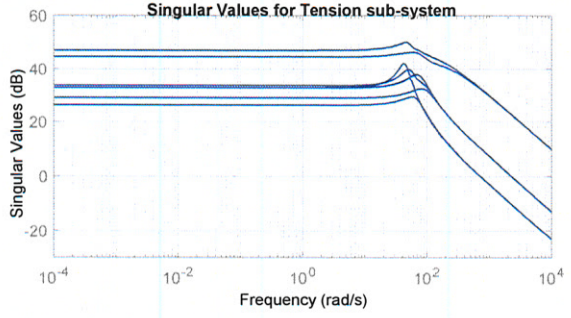

Figure 6-2: Singular values for the model of 6-6 showing the maximum gain of the system of each output for all linear combinations of the input in a certain frequency range.

Relative Gain Array To verify that the inputs and outputs are close to being decoupled, the RGA can again be used. Once more, a frequency of $\omega = 0.1$ rad/s is used for its computation:

For ease of reading, the values closest to 1 are presented in bold. As they are all on the diagonal of the RGA, the inputs and outputs shall be assumed as decoupled for the design of the controller. In other words, input 1 will be assumed to only affect output 1 and so forth. Note that this is not *actually* the case however and that any controller design that results from this analysis might be subject to changes depending on its performance. These changes are not expected to be large and are more likely to occur for the hoist cables than the others, based on the RGA. Furthermore, the RGA is computed for higher frequencies as well where it only gets closer to identity.

6-2 Kinematic model analysis

In the preceding half of the analysis of the model, it was found that that the Jacobian was of rank 5 and that the associated DOF of roll means that the system is not capable of applying a moment on the roll using the 8 cables. In this half of the model analysis, on kinematics, the Jacobian will therefore be reduced by omitting the row that corresponds to roll, i.e $\mathbf{J}^T \in \mathbb{R}^{8\times5}$. In fact, the loss of rank is referred to as a *singularity* in robotics and indicates for which configurations the system loses control over a certain DOF, as it does for roll. In this section it is researched, among other things, if there exist more configurations that cause loss in rank. This information is then used to construct a workspace of the that shows the extent of possible poses.

6-2-1 Singularities

The phenomenon of a singularity is an important one in robotics. In serial robots this typically occurs when two or more joints align, making them redundant in that configuration. Mathematically, the Jacobian loses rank when the robot is in its singular configuration and this can occur for serial robots as well as parallel robots. In parallel robots however, the singular configurations are less intuitive since the joints are coupled. Furthermore, there are two different types of singularities for CSPM in particular. Type I is the Jacobian rank deficient singularity just mentioned, or *Jacobian singularity*. A type II singularity occurs when the Jacobian is full-rank but the tension solution gives negative tensions, as described in the previous section. This is referred to as a *force-closure singularity* by Diao in [26].

Jacobian singularities To find the type I singularities of the , one must find the configuration where the Jacobian looses rank. This means that for any such configuration the projected image of the joint-space onto the task-space results in a lower than full-rank

dimension, i.e. there exist no combination of cable movement that results in the movement of the associated degree-of-freedom to the drop in rank. To check for these configurations, normally the determinant of the Jacobian is checked for when it becomes zero, i.e. $\det(\mathbf{J}) = 0$. However, since the is a redundant system and the Jacobian is non-square, instead it should be checked when:

$$\det(\mathbf{J}^T\mathbf{J}) = 0 \tag{6-10}$$

This can either be done analytically or numerically. An analytic approach in this case is a highly tedious task since it requires to solve (6-10) for the pose $\mathbf{x}$. A numeric approach needs only to evaluate the equation and can show for a mesh of poses where it approaches a singularity. This can either be done by checking whether (6-10) approaches zero, or by defining a condition variable κ as the ratio between the largest and smallest singular values of $\mathbf{J}^T$, as in Pusey et al. [27] and section 6-1, such that when the smallest singular value approaches zero (which is equivalent to (6-10)), κ approaches infinity.

$$\kappa = \frac{\sigma_{max}}{\sigma_{min}} \tag{6-11}$$

Force-closure singularities To find the type II singularities, one must find the configurations where the desired wrench can no longer be achieved by only positive tensions. Since the wrench and tension are related by the transposed Jacobian as shown in (2-13), this comes down to verifying if the desired wrench lays within the *positive span* of $\mathbf{J}^T$. The positive span of $\mathbf{J}^T$ is the conic subspace that is formed by *any* basis of $\mathbf{J}^T$ scaled with only positive values for $\mathbf{t}$, as adapted from Regis [28]. For this analysis, the Jacobian is assumed to always be full rank (i.e. the configuration is not in a Jacobian singularity). This means that a basis $\mathbf{J}_B$ of $\mathbf{J}^T$ that spans $\mathbb{R}^5$ can always be found. This method has been proposed by Diao et al. in [29]. To illustrate this idea further, consider that the desired wrench can be written as the linear combination of the columns of $\mathbf{J}^T = [\mathbf{j}_1 \quad \mathbf{j}_2 \quad \cdots \quad \mathbf{j}_8]$ and the tension entries of $\mathbf{t} = [t_1 \quad t_2 \quad \cdots \quad t_8]^T$ to yield:

$$\mathbf{w}_{des} = \mathbf{j}_1 t_1 + \mathbf{j}_2 t_2 + \cdots + \mathbf{j}_8 t_8 \tag{6-12}$$

Any five linearly independent vectors of $\mathbf{J}^T$ form a basis. If the desired wrench $\mathbf{w}_{des}$ lies within the positive span of one of these basis, it is feasible. To test if a wrench lies within the positive span, the basis $\mathbf{J}_B$ is transformed to the identity matrix such that when the desired wrench is transformed by applying the same transformation matrix, it can be achieved by positive cable tensions if and only if the result is strictly non-negative. Note that this transformation matrix is simply the inverse of the basis of the transposed Jacobian, i.e. $\mathbf{J}_{Bi}^{-1}$, where $\mathbf{J}_{Bi}$ denotes the i^{th} basis of $\mathbf{J}^T$.

To get a clearer intuition of this method, a two-dimensional example is shown in figure 6-3, where the Jacobian is only a 2x3 matrix. Note that the positive span is further limited to only include tensions lower than the maximum allowed tension $\mathbf{t}_{max}$. *In fact, for any specific configuration, when the desired wrench is feasible, i.e. is a member of the positive span, it can always be achieved by some tension derived from the general tension solution:*

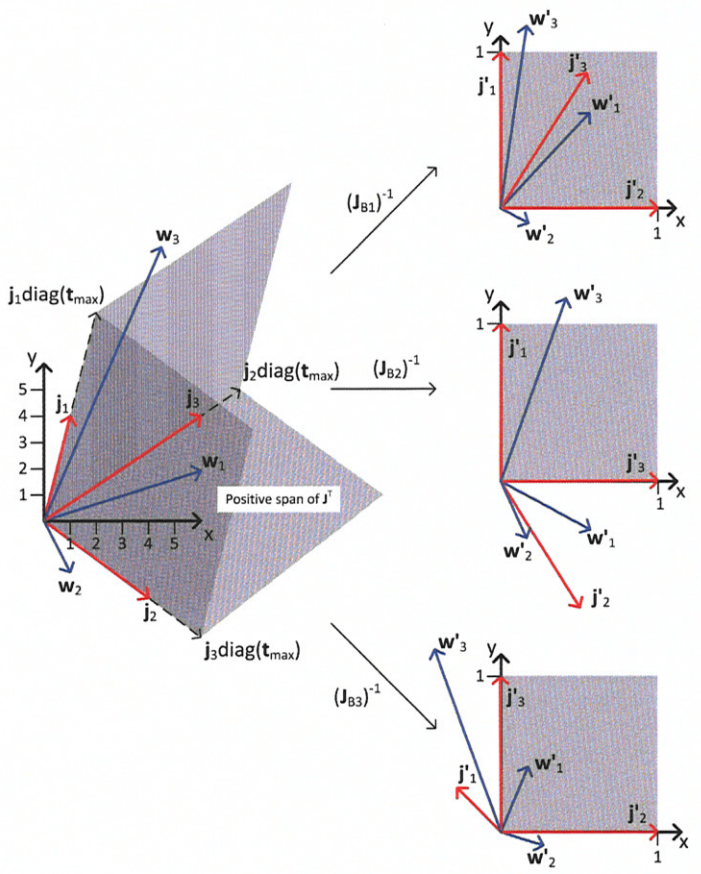

Figure 6-3: A two-dimensional example of the positive span of $\mathbf{J}^T$. The three possible basis here ($\mathbf{J}_{B1} = span\{\mathbf{j}_1,\mathbf{j}_2\}, \mathbf{J}_{B2} = span\{\mathbf{j}_1,\mathbf{j}_3\}, \mathbf{J}_{B3} = span\{\mathbf{j}_3,\mathbf{j}_2\}$) are multiplied by the maximum tension for each cable $\mathbf{t}_{max}$ and then transformed to the identity matrix by their inverse, i.e. $\mathbf{j'}_i = \mathbf{J}_{Bi}^{-1}\mathbf{j}_i \text{diag}(\mathbf{t}_{max})$. This way, the positive span only includes strictly non-negative vectors with entries less than one. Three possible desired wrenches are shown where $\mathbf{w}_1$ is a feasible wrench and $\mathbf{w}_2$ and $\mathbf{w}_3$ are not feasible. It can be observed that for all possible basis, the positive span includes $\mathbf{w}_1$ in two cases but does *not* include $\mathbf{w}_2$ nor $\mathbf{w}_3$ in *any* case. Thus, $\mathbf{w}_2$ and $\mathbf{w}_3$ can be said to fall outside of the positive span of $\mathbf{J}^T$. In fact, the specific configuration that defines the Jacobian is said to be force-closure singular for all desired wrenches that fall outside of its positive span.

$$\mathbf{t}_{des} = \mathbf{N}\boldsymbol{\lambda} - \left(\mathbf{J}^T\right)^{\dagger}\mathbf{w}_{des} \quad \text{Where} \quad \mathbf{0} \leq \mathbf{t}_{des} \leq \mathbf{t}_{max} \tag{6-13}$$

6-2-2 Analysis of static workspace

Using information about the tension solution of section 5-1, the limitation on roll found in section 6-1-1 and the occurrences of singularities defined in the previous section, a final analysis of the possible configurations of the will be carried out known as the Workspace (WS) of the system. This is often done for such systems as seen in Pusey et al. [27], Arsenault et al. [30] and Berti et al. [24]. The goal of this analysis is to obtain the set of poses that the can assume for which no negative cable tensions are required. A distinction is made between the workspace that is obtained using only the *pseudo-inverse tension solution* of (5-1), which is a single solution, and the workspace that is obtained using the *general tension solution* of (6-13), where all possible solutions are considered.

Method of workspace computation The workspace is a purely static analysis which only takes into account gravity as an external force on the . The desired wrench is therefore opposite to the gravity force, i.e $\mathbf{w}_{des} = [0 \quad 0 \quad -mg \quad 0 \quad 0 \quad 0]^T$. The workspace is computed only for poses, the is fixed to the reference frame. First, the workspace using only the pseudo-inverse solution is computed by evaluating (5-1) for a mesh of poses and included only those poses that can be achieved using all positive cable tensions. The algorithm is stated in pseudo code in Algorithm 1.

Algorithm 1 Workspace algorithm for Pseudo-Inverse Tension Solution

$\mathbf{w}_{des} = [0 \quad 0 \quad -mg \quad 0 \quad 0 \quad 0]^T$
for x = 0 : 0.025 : 0.35 **do**
  for y = 0 : 0.025 : 0.35 **do**
    for z = 0.4 : 0.2 : 4 **do**
      for θ = -1.3 : 0.04 : 1.3 **do**
        for ψ = -0.8 : 0.02 : 0.8 **do**
          $\mathbf{x}_{SB} = [x \quad y \quad z \quad \theta \quad \psi]^T$
          $\mathbf{t} = -\left(\mathbf{J}(\mathbf{x}_{SB})^T\right)^{\dagger}\mathbf{w}_{des}$
          if $\mathbf{t} > 0$ && $\mathbf{t} < \mathbf{t}_{max}$ **then**
            $WS = \mathbf{x}_{SB}$
          end
      ⋱
end

Where WS contains all poses that can be achieved with positive cable tensions. Notice in algorithm 1 that the WS is only computed for positive values of each of the translation DOF (x, y, z). The reason for doing this for heave (z) is clear since the only operates below the . For surge (x) and sway (y), the reason is to decrease computation time of the workspace. This is possible because the system is symmetric in these directions. Therefore, the algorithm only needs to compute a quarter of the workspace in these directions, which can then simply

be copied for the other 3 quarters of the entire workspace. Naturally, the rotations need to be computed fully. Next, the workspace using the general tension solution of (6-13) can be computed using the algorithm on force-closure singularities presented in 6-2-1:

- Define a new 5x5 matrix $\mathbf{J}_B$ that is obtained from linearly independent columns of $\mathbf{J}^T$ and multiply by a diagonal matrix of maximum tensions $\text{diag}(\mathbf{t}_{max})$. This is always possible since it is assumed the configuration is not in a Jacobian singularity.
- Define the transformation matrix that transforms the basis $\mathbf{J}_B$ to the 5x5 identity matrix as the inverse of $\mathbf{J}_B$.
- Apply this transformation to the desired wrench, i.e $\mathbf{w}' = \mathbf{J}_B^{-1}\mathbf{w}_{des}$
- The desired wrench is feasible if and only if $\mathbf{w}'$ has strictly non-negative entries for any basis of $\mathbf{J}^T$ *and* values less than one for each entry, i.e. $0 \leq \mathbf{w}' \leq 1$. If negative entries or entries larger that one occur for *all* basis, the configuration is said to be force-closure singular for that specific wrench.

The algorithm is given in pseudo code in Algorithm 2. *Note that since only 5 DOF are to be controlled, a minimum of 5 cables are required to fully constrain the movement of these 5 DOF (gravity acts as the sixth cable to satisfy $m_c = n_d + 1$ with m_c the amount of cables and n_d the DOF, from Berti et al. [24]), the algorithm essentially virtually removes 3 different cables each iteration and checks if the desired wrench can be achieved using any combination of the 5 remaining cables.*

Algorithm 2 Workspace algorithm for General Solution

$\mathbf{w}_{des} = [0 \quad 0 \quad -mg \quad 0 \quad 0 \quad 0]^T$
for x = 0 : 0.025 : 0.35 **do**
  for y = 0 : 0.025 : 0.35 **do**
    for z = 0.4 : 0.2 : 4 **do**
      for θ = 0 : 0.04 : 1.3 **do**
        for ψ = 0 : 0.02 : 0.8 **do**
          $\mathbf{x}_{SB} = [x \quad y \quad z \quad \theta \quad \psi]^T$
          for i = 1 : 6 **do**
            for j = (i+1) : 7 **do**
              for k = (j+1) : 8 **do**
                $\mathbf{J}(\text{i},:) = 0; \quad \mathbf{J}(\text{j},:) = 0; \quad \mathbf{J}(\text{k},:) = 0$
                $\mathbf{J}_B(\mathbf{x}_{SB}) = \mathbf{J}(\mathbf{x}_{SB})^T\text{diag}(\mathbf{t}_{max})$
                if $\text{rank}(\mathbf{J}_B(\mathbf{x}_{SB})) == 5$ **then**
                  $\mathbf{w}_B = \mathbf{J}_B^{-1}(\mathbf{x}_{SB})\mathbf{w}_{des}$
                  if $\mathbf{w}_B >= 0$ && $\mathbf{w}_B =< 1$ **then**
                    $WS = \mathbf{x}_{SB}$
                  end
                ⋱
end

Where for each configuration, all possible 5x5 basis of the Jacobian are constructed and used for the transformation of $\mathbf{w}_{des}$ to its identity form $\mathbf{w}_B$. For $\mathbf{w}_B$ it is then checked whether its entries fall within 0 and 1. If so, the configuration is added to the workspace.

Workspace results The algorithms of the previous section return the set of configurations for which the conditions of each approach hold. This means that an array of coordinates is obtained that identify the poses that the can assume that satisfy the respective constraints of each approach. This array can be visualized by interpolating between the individual points and plotting the surface that arises. Figure 6-4 shows both the resulting workspaces for the pseudo-inverse tension solution of (5-1) and general tension solution of 6-13, for translations and rotations separately. The workspace that corresponds to the pseudo-inverse tension solution is yellow and the blue one belongs to the general tensions solution. The figure shows the maximum values that the can assume under the given conditions, for clarity they are given in table 6-1. These limits (and figure) show that the workspace based on the general tension solution is larger than the one based on the pseudo-inverse solution.

Table 6-1: Workspace limits under the conditions given in the figure, i.e. Translations for $[\theta \quad \psi]^T = [0 \quad 0]^T$ and Rotations for $[x \quad y \quad z]^T = [0 \quad 0 \quad 2m]^T$

Workspace limits	Pseudo-Inverse Solution [m]/[rad]	General Solution [m]/[rad]
Max Surge (x)	0.075	0.25
Max Sway (y)	0.2	0.275
Max Pitch (θ)	1.1	1.24
Max Yaw (ψ)	0.5	0.74

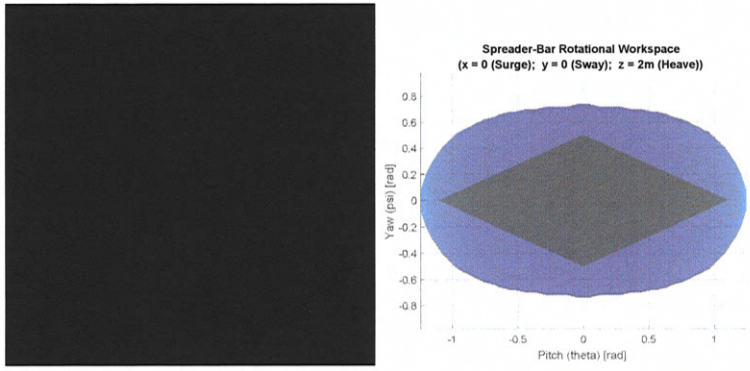

Figure 6-4: Left: Translation workspace of the . The yellow rectangular shaped workspace belongs to the *pseudo-inverse* tension solution and the blue cylindrical workspace to the *general* tension solution. **Right:** Rotational workspace of the for the central configuration (as drawn in the left figure). Again, yellow is the *pseudo-inverse* tension solution and blue the *general* tension solution

To check for singularities, the condition number κ is checked. Specifically, the maximum values for the workspace of the general solution is given in table 6-2, as this also includes the workspace for the pseudo-inverse solution. A singularity is indicated by a singular value that

goes to zero, such that κ of (6-11) goes to infinity. *The maximum values of κ are relatively small, meaning that no singularity is present in the workspace of the for its central position.*

Table 6-2: Jacobian maximum condition number of entire workspace for Translation and Rotation using the general solution

Workspace	Translation	Rotation
$\max(\kappa)$	41.3339	68.8670

Chapter 7

Controller design

This chapter will highlight the design of the controller, consisting of the
MC FC TD

will be designed such that its bandwidth is at least 10 times higher than the MC in order for the cables to appear stiff. Finally, the TD ensures that the desired wrench of the MC results in cable tensions that are within their minimum and maximum bounds.

7-1 Motion controller

For the design of the motion controller, the motion sub-system of 6-3 will be used for which it was found that the inputs and outputs are perfectly decoupled, given that roll is excluded from control. The transfer function between each wrench input and position output can be plotted as a bode diagrams which in turn can be used to design the controller. Figure 7-2 shows the magnitude and phase plots for each input/output pair in a single figure. Note that the magnitude plot closely resembles the singular value plot of figure 6-1. This makes sense because of the decoupled nature of most of the system.

Note that the system is intrinsically unstable due to the -180 degree phase shift at cross-over frequency ω_c. This means firstly that phase needs to be added around the cross-over frequency. To add phase, at least a derivative control action $K_{d,m}$ is required in combination with a proportional gain $K_{p,m}$. A small integrative action $K_{i,m}$ will also be included to eliminate steady-state error. Thus, the controller will be of the Proportional-Integral-Derivative (PID) form:

$$C_m(s) = K_{p,m} + \frac{K_{i,m}}{s} + K_{d,m}s \tag{7-1}$$

Where s represents the Laplace complex variable. Each DOF is then tuned independently where the bandwidth is maximized while keeping resonances attenuated. This is done by

writing (7-1) into a form where the gain and frequencies of adding phase can easily be chosen, given in (7-2). Where $T_{i,m}$ is the frequency corresponding to the integrative action and $T_{d,m}$ the frequency of the derivative action, i.e. where phase is added.

$$C_m(s) = K_{p,m}\left(1 + \frac{T_{i,m}}{s} + \frac{s}{T_{d,m}}\right) \tag{7-2}$$

Design procedure The design procedure for each DOF is that $T_{d,m}$ is set at a frequency *before* the crossover frequency such that there is at least 60 degrees of Phase Margin (PM) at the crossover. Then K_p is increased such that there is at least 6dB of Gain Margin (GM) at the -180 degrees phase crossing close to the crossover frequency. Finally, $T_{i,m}$ is increased such that the gain at the low frequency -180 degrees phase crossing is at least 20dB. *The values of $T_{d,m}$, K_p and $T_{i,m}$ are iteratively changed until the best trade-off between these requirements is met.*

The resulting closed-loop behaviour is plotted in figure 7-2, along with the plant and open-loop bode for each DOF separately. The step response of each of the DOF is also shown in figure 7-3. For both the bode and the step response, the performance parameters are given in table 7-1, where the Band-Width (BW), GM and PM are shown and t_s is the settling time in seconds.

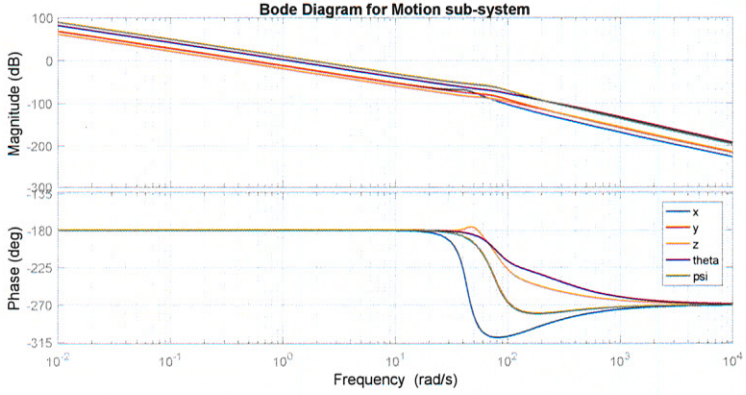

Figure 7-1: Bode plot for all 5 controllable DOF transfer functions of the motion sub-system. Each bode plot therefore represents the frequency behaviour of each DOF with respect to its corresponding input.

[redacted]

Table 7-1: Motion Controller parameters and performance. Note that the gain margin (GM) for heave and pitch (z, θ) are not defined as there is no -180 degrees crossing after the cross-over frequency.

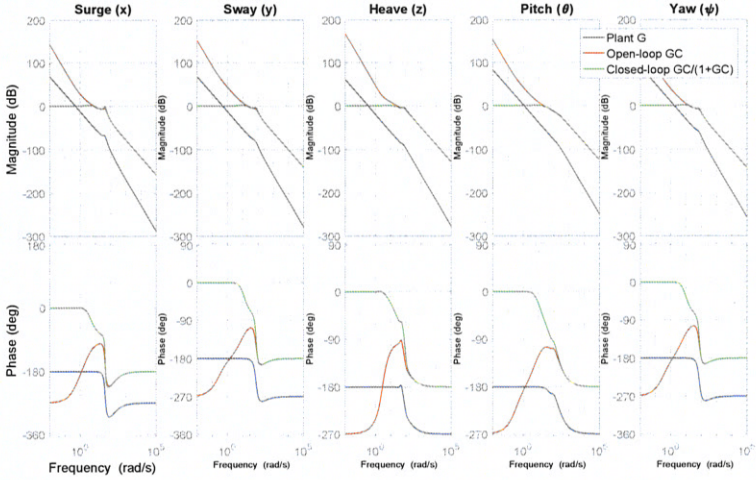

Figure 7-2: Bode plots for all 5 controllable DOF transfer functions. The plant, open-loop controller and closed-loop bodes are shown in blue, red and green respectively. Exact values on bandwidth (BW), gain margin (GM) and phase margin (PM) are found in table 7-1

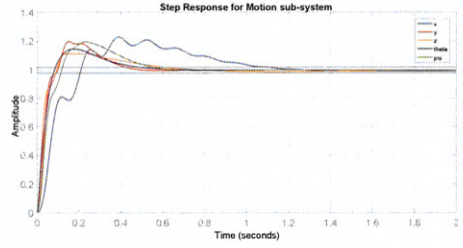

Figure 7-3: Step Response for all 5 controllable DOF transfer functions. The settling time bounds are plotted by the horizontal black lines and are defined as a 2% deviation from the setpoint.

7-2 Force Controller

For the design of the force controller, the tension sub-system of 6-7 will be used for which it was found that the inputs and outputs are nearly decoupled. The transfer function between each torque input and cable force output can be plotted in a bode plot which will again be used to design the force controllers. Figure 7-4 shows these plots. Due to the symmetry of the system, the controllers for the hoist, controllers for surge and controllers for sway actuators, can be identical. This is apparent in figure 7-4 where the bode plots of the symmetrical torque-to-tension systems perfectly overlap, and only three distinct plots are visible. Note that in this case, the magnitude plots deviate somewhat from the singular value plot of figure 6-2, as is expected from the fact that the inputs are not perfectly decoupled from the outputs.

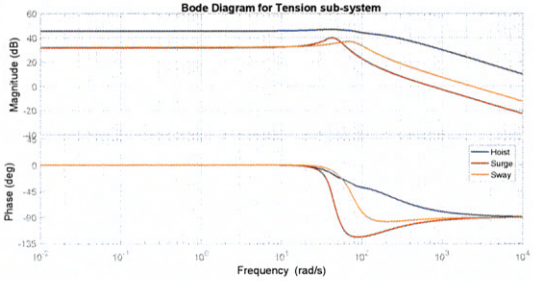

Figure 7-4: Bode plot for all 8 inputs and outputs of the tension sub-system where the bode plots for the hoist cables overlap with one another, as well as the bode plots for the surge and sway cables, leaving only three distinct bode plots.

Note that the phase here does not reach -180 degrees for the entire frequency spectrum. No additional phase is required, eliminating the need for a derivative control action. It is still desirable to have higher gain for lower frequencies however, which means an integrative control action $K_{i,f}$ is used in combination with a proportional gain $K_{p,f}$. This means finally that a Proportional-Integral (PI)-controller will be implemented of the form:

$$C_f(s) = K_{p,f} + \frac{K_{i,f}}{s} \tag{7-3}$$

Each cable system is again tuned independently where the BW is desired to be at least a factor of 10 larger than the maximum BW of the motion controller. Once more, (7-3) can be written in terms of physically interpretable variables, given in (7-4). Where $T_{i,f}$ is the frequency corresponding to the integral action of the controller.

$$C_f(s) = K_{p,f}\left(1 + \frac{T_{i,f}}{s}\right) \tag{7-4}$$

Design Procedure The design procedure here is different for the surge/sway cables and the hoist cables. For the surge and sway cables, $T_{i,f}$ is set at a frequency *before* their resonance peak such that the phase drop does not add much to the lowest point in phase in order to

prevent coming near -180 degrees. Then, $K_{p,f}$ is changed such the BW does not exceed 1000 rad/s, since there is some coupling between the inputs and outputs and there is a risk of exciting internal dynamics. For the hoist cables the phase barely drops so that $T_{i,f}$ can be set at a higher frequency such that the open-loop response acts almost as a pure integrator. Then $K_{p,f}$ is changed to balance BW and phase drop in the closed-loop response.

Figure 7-5 shows the open-loop and closed loop bodes for each cable system and figure 7-6 shows the step responses for the controller parameters given in table 7-2. The table further provides the performance parameters.

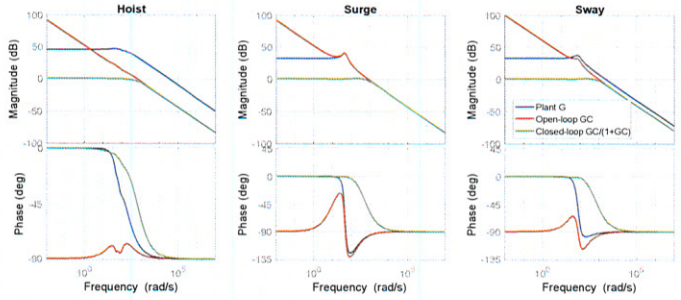

Figure 7-5: Bode plots for each cable tension transfer function. The plant, open-loop and closed-loop bodes are shown in blue, red and green respectively. Exact values on bandwidth (BW), gain margin (GM) and phase margin (PM) are found in table 7-2

[redacted]

Table 7-2: Force Controller parameters and performance. Note that the controller gains might need to be adjusted slightly in the non-linear model because the system is not fully decoupled.

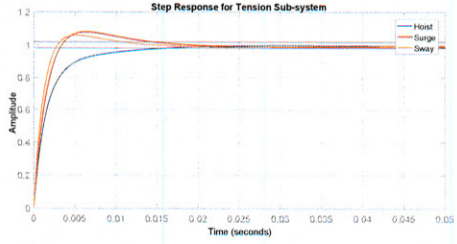

Figure 7-6: Step responses of the force controllers. Settling time bounds are plotted by the horizontal black lines and are defined as a 2% deviations from the setpoint.

7-3 Tension Distribution

The final step in controlling the is the TD that transforms the desired wrench that is obtained from the MC to desired cable tensions for the FC. Two possibilities have been presented for this purpose, the Pseudo-inverse tension solution (5-1) and general tension solution (6-13). Although the latter has shown to likely yield better results in terms of workspace and possibly preventing negative tension, its implementation is highly complex and computationally non-efficient (see Appendix ??). The former on the other hand is a highly efficient and simple solution. For this reason, the Pseudo-inverse tension solution is used. *However, it has become clear that this solution alone is not sufficient as it can cause negative tension for certain configurations as was shown in figure 6-4.* The easiest solution to this problem is to saturate the solution to a minimum tension t_{min} for each cable. The force controller then ensures that cable tensions do not fall below this minimum value. The disadvantage is that the resulting wrench acting on the is not the actual desired one which might cause a drop in performance. The minimum value of the force in each cable is set to $t_{min} = 2N$. This is determined such that overshoot in the force controller does not cause negative tension. The saturation block also implements limits for maximum cable tensions.

An adjustment is further made to the Pseudo-inverse tension solution to prevent any control action on roll. Since roll was found to be singular in the Jacobian, the associated column is set to zero in the transposed Jacobian of the tension solution before it is inverted. This is necessary since the inverse will otherwise result in values approaching infinity.

7-4 Final Controller

The control strategy for controlling the designed in this chapter, with a tension distribution based on the pseudo-inverse of the Jacobian that is saturated to the minimum and maximum tensions allowed in each cable to prevent cable slack and cables breaking respectively. The controller is shown in full in figure 7-7.

[redacted]

Figure 7-7: Block diagram of the controller for the (see figure 2-3) including the PID motion controller, saturated pseudo-inverse TD and PI force controller.

Part III

Results, Discussion and Recommendations

Chapter 8

Simulations

This chapter will present the simulation results of the controller that was designed in the previous chapter. The goal of these simulations is two-fold. It is firstly a verification of the simulation model in terms of its purpose, i.e. how does the model behave when controlled; is its behaviour realistic and can the results be trusted. Secondly, the performance of the controller is evaluated in terms of the position error with respect to the requirements and of the cable tension behaviour.

8-1 Simulation method

The simulation is done in . The controller will be subjected to *two* scenarios where in each case a trajectory is made available that is based on the JONSWAP spectrum [1]. These trajectories are periodic signals on each of the DOF of *both* poses where their masses, shapes and wave reflection between the vessels have been taken into account for the computation of these trajectories. The first trajectory simulates calm sea conditions and the second trajectory simulates the worst-case sea conditions that were already given for the *real* system in figure 1-3. *The simulations will only show a portion of the actual lengths of time that these conditions normally have since the computation for several hours of these conditions is highly time-consuming.*

The operating point in all cases is again $\mathbf{x}_{SB} = [0 \quad 0 \quad 2\text{m} \quad 0 \quad 0 \quad 0]^T$ since this is the operating point for which the controller was designed. A desired error of 0.2m is defined for heave, i.e the at a distance of 0.2m above it. This firstly depicts a more realistic scenario as tracking on the real system is activated while the is still above the , and secondly shows how well the controller still performs when it is further away from its operating point.

8-2 Simulation results for Trajectory I

The first simulated trajectory is one of calm weather conditions, meaning that the maximum wave frequency is on the *lower* side of the spectrum and the angle of attack is 90 degrees. Figure 8-2 shows the scenario for this trajectory where the *maximum* period for a wave is given based on the parameters of table 1-3, i.e. $Ts = \frac{1}{0.21Hz} = 4.76s$. The significant wave height is still based on the 4.5m maximum for the *real* system, resulting in the values given in table 1-3, but high waves occur less often. The angle of attack of 90 degrees further means that the waves are attenuated by before they reach the .

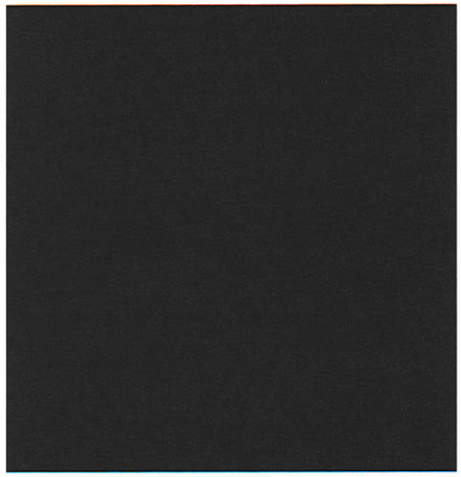

Figure 8-1: Scenario for trajectory I of calm weather conditions based on the JONSWAP spectrum with maximum frequency of 0.21Hz, significant wave height based on the 4,5m of the *real* system and angle of attack of 90 degrees. Note that the given period for the wave is the *maximum* that occurs for these conditions.

8-2-1 Position tracking and motion compensation

The simulation data is shown in figure 8-1 for each DOF where both the trajectory (the reference) and pose are plotted. *Note that while the motions are not plotted, the is actively compensating for its motions and the results include these motions.* Furthermore, the error signal is plotted where translations and rotations are shown separately. Roll is not controlled and therefore shows relatively large errors, but is stable nonetheless.

A quantitative measure for performance is given in table 8-1 where the maximum error and Root Mean Square (RMS) error are given respectively for each DOF. It shows that for all the controllable DOF the performance of surge is the lowest, but still falls well within the required 2 mm for both maximum and RMS errors. Therefore, all controllable DOF perform exceptionally well. Naturally, since roll is not controlled it does not track its reference and while the errors are larger than the requirements, they are still small in absolute terms and the system remains stable.

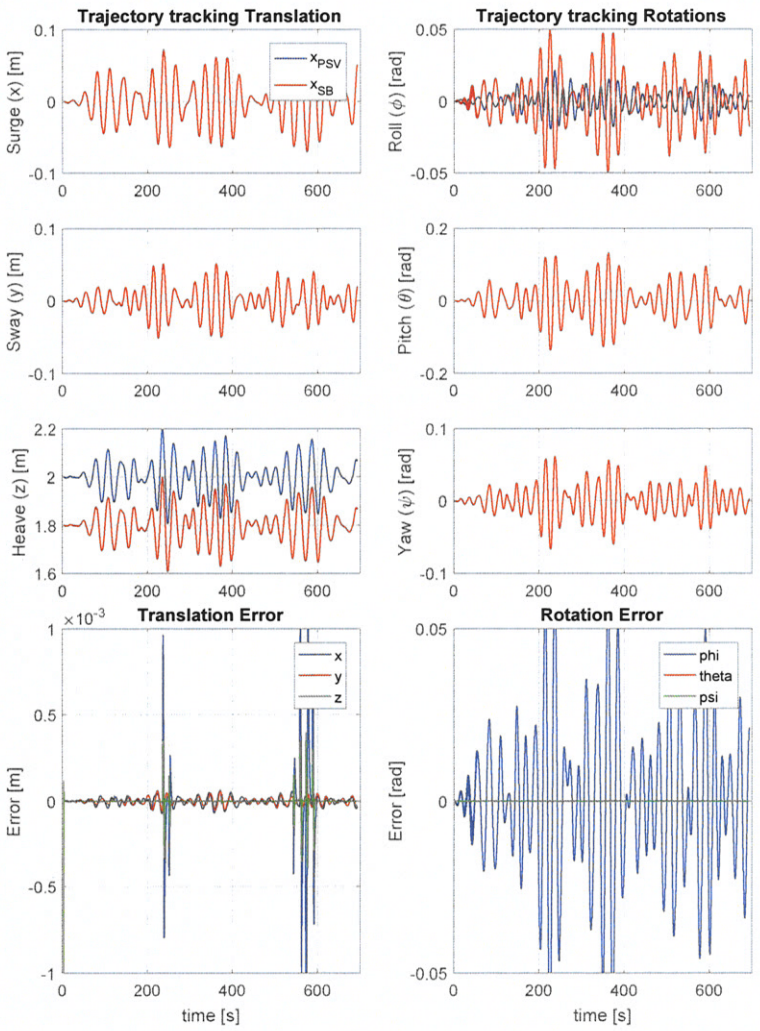

Figure 8-2: Controller results of tracking each controllable DOF simultaneously (excluding roll) for calm weather conditions. Note that the heave is intentionally offset by 0.2m such that the tracks the from above. Further note that the figure only shows the trajectories for the motions is included in these results

Table 8-1: Maximum and RMS error values for trajectory tracking of all controllable DOF for trajectory I of calm weather conditions

DOF	max error [mm]/[rad]	RMS error [mm]/[rad]
Surge (x)	1.414	0.158
Sway (y)	0.06335	0.020845
Heave (z)	0.397	0.0535
Roll (ϕ)	0.0682	0.022815
Pitch (θ)	3.14e-05	4.323e-06
Yaw (ψ)	4.822e-05	1.54e-05

8-2-2 Cable tensions for trajectory I

The performance of the force controller can be derived from the cable tensions, which are shown in figure 8-3 for the same simulation. These tensions correspond to the motions in figure 8-1. Most notable about the cable tensions for the calm weather conditions is the fact that they are smooth. There are no oscillations, even for the regions where the saturation limits the cable tensions. this can be clearly observed between the 500 and 600 seconds mark for both surge cables. The effect this has on the position in negligibly small. This shows clearly that the controller manages to keep all cable tensions positive throughout operation for weather conditions of this category.

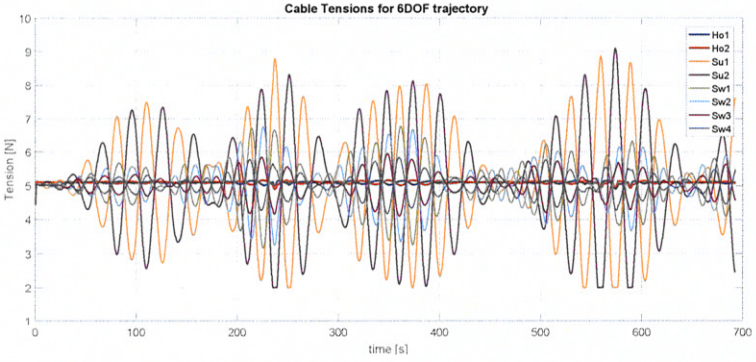

Figure 8-3: Cable tensions for trajectory tracking under calm weather conditions. The tension can be seen to saturate between 500 and 600 seconds where the force controller follows the minimum allowed tension rather than the tension solution.

8-3 Simulation results for Trajectory II

The second simulated trajectory is for worst-case weather conditions, meaning that the maximum wave frequency is on the *higher* side of the spectrum and the angle of attack is 225

degrees. Figure 8-4 shows the scenario for this trajectory where the maximum period for a wave is given based on the parameters of table 1-3, i.e. $Ts = \frac{1}{1.16Hz} = 0.862s$. The significant wave height is still based on the 4.5m maximum for the *real* system, resulting in the values given in table 1-3, but high waves occur more frequently. The angle of attack of 225 degrees further means that the waves are reflected by before they reach the , resulting in high dynamic behaviour for the latter.

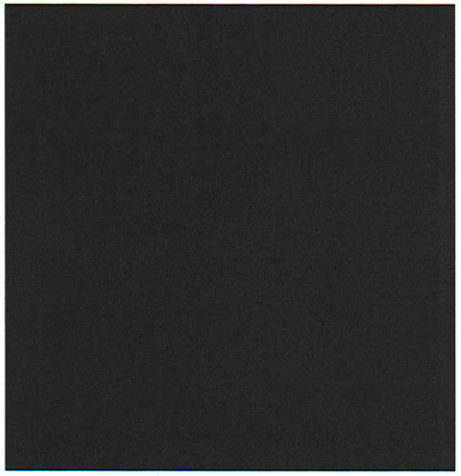

Figure 8-4: Scenario for the second simulated trajectory of worst-case weather conditions based on the JONSWAP spectrum with maximum frequency of 1.16Hz, significant wave height based on the 4,5m of the *real* system and angle of attack of 225 degrees. Note that the given period for the wave is the *maximum* that occurs for these conditions.

8-3-1 Position tracking and motion compensation

The simulation data is shown in figure 8-5 for each DOF where both the trajectory (the reference) and pose are plotted. *Note that while the motions are not plotted, the is actively compensating for its motions and the results include these motions.* Furthermore, the error signal is plotted where translations and rotations are shown separately. Roll is not controlled and is seen to occasionally exhibit large error spikes, but is stable nonetheless.

Again, the maximum and RMS error values are given in table 8-2. *Note that the figure only shows 80 seconds of simulated trajectory where in fact 200 seconds are actually simulated. This is done to preserve the readability of the figure.* For the calculations of the error values, the entire simulated date is taken. Surge and roll are again the lowest performing DOF. For translations, the requirements are not met except in sway where the RMS error is lower than 2 mm. However, the RMS error values are still small in absolute terms. In this case however, the rough conditions can occasionally cause large error spikes which can also be seen in figure 8-5 around the 70 second mark. These spikes are responsible for the high maximum errors. For the rotations, the requirements are still met, except again in roll.

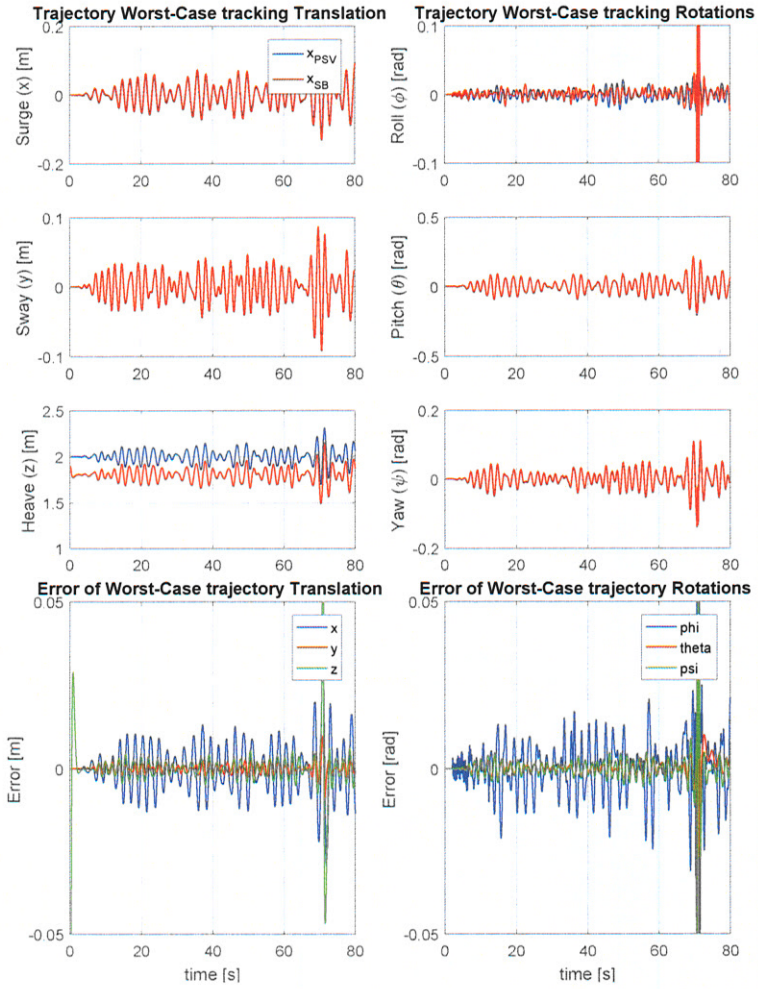

Figure 8-5: Controller performance of tracking each controllable DOF simultaneously (excluding roll) for worst-case weather conditions. Note that the heave is intentionally offset by 0.2m such that it tracks the from above. Further note that the figure only shows the trajectories for the but compensation for motions is included in these results

Table 8-2: Maximum and RMS error values for trajectory tracking of all controllable DOF for worst-case weather conditions

DOF	max error [mm]/[rad]	RMS error [mm]/[rad]
Surge (x)	33.75	8.574
Sway (y)	9.74	1.52
Heave (z)	79.4	5.73
Roll (ϕ)	0.645	0.02545
Pitch (θ)	0.0804	0.00306
Yaw (ψ)	0.0814	0.0038

8-3-2 Cable tensions for trajectory II

The cable tensions for the worst-case conditions are shown in figure 8-6. The tension is mostly smooth but can be seen to oscillate for short periods of time for mostly the hoist cables. The force controller is not fast enough to prevent negative tension for these cases. However, stability is not lost.

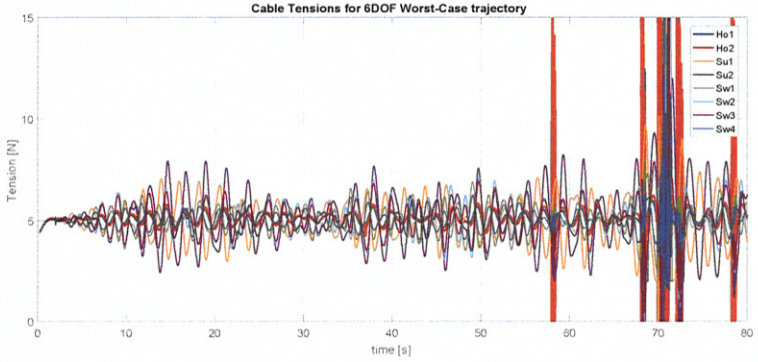

Figure 8-6: Cable tensions for trajectory tracking under worst-case weather conditions. The tension can be seen to oscillate for certain motions of where the force controller is not fast enough to keep the tension at the minimum allowed value of 2N. Here, negative tension occurs for short periods of time.

Chapter 9

Discussion & Recommendations

This chapter will again state the sub-problems and research questions and answer them as completely as possible based on the information that is gathered from this thesis and the results that it has produced. First the research questions shall be answered since they relate directly to the contents of this thesis. Then the sub-problems are discussed, which rely in part on some of the answers to the research questions and form the bridge between the results from this thesis and answering the general problem statement for the *actual* . the latter will then be discussed in terms of the contribution that this thesis has made in solving it. Finally, some recommendations and possible improvements are given to parts of this thesis and to future work.

9-1 Research question answers

In this section the research questions that were asked at the start of this thesis will be answered. The question will first be re-iterated and then an answer is provided

Which modelling approach balances performance and computation time? For this question, three sub-question are first answered:

1. **Which dynamics need to be captured by the model?** In chapter 2 the model is derived where the system is divided into three different dynamic parts, namely:

These three separate dynamic systems are then combined by kinematic constraints

2. **Does the model include all the challenges of the system?** In order to obtain a model that could be used to test controllers that could potentially solve the challenges that the system exhibits, the challenges need to be present in the model. Several challenges for which no clear solution exists have been identified and are included in the model.
   - **Moving in 6 DOF**: The model includes an extra frame for the can move independently with respect to the fixed reference frame. The movements are considered as determined and only effect the cable lengths, which in turn effects the tensions and therefore the motions.
   - **Over-actuated:** This is modeled by the Jacobian $\mathbf{J} \in \mathbb{R}^{8\times6}$, which is non-square because of the redundancy.
   - **Occurrence of negative tension:** The cable model that is used to model the cable tensions can give negative tensions. A saturation block is therefore placed in the model that limits the tensions to zero. Thus negative tension is modeled. However, the loss of tension in the actual system causes highly non-linear behaviour which is unpredictable. Therefore, the model is still only assumed valid for positive tensions.
   - **Non-linear effect:** To include the most prominent non-linear effects of the system into the model, the cables are accurately identified and verified.
3. **What is the computation time of the simulation?** Using a computer with a 3.2GHz processor, the model (without controller) is verified to run at a speed of 2.077 times actual time. This is deemed fast enough to state that the model is well-suited to be used for testing and designing controllers.

Therefore, the modeling approach that was used in this thesis is deemed suited to balance performance and computations time sufficiently since it includes the most prominent dynamics of the system, captures all the problems that the controller needs to deal with and is fast enough to allow for quick testing.

How to verify the model? For the model to be used for testing and designing controllers that can be used on the test-bed set-up, it needs to be physically accurate to the system. For this reason, a verification is carried out. This is done by the use of an external motion capturing system called . This system can accurately measure the motions of the which have been used to verify the model by using the same input on both the system and the model and comparing the outputs.

- **How accurate does the model need to be?** For the comparison between the model and actual system, the Variance Accounted For (VAF) was used which yielded values between 91.4 and 99.9877% in the most relevant direction and a mean VAF of 89.5% for all translations (rotations are not excited, refer to Section 4-2 and Appendix ??). There exist no requirements for VAF values that ensure the validity of the model, but since the measure is normalized between 0 and 100, the closer to 100 the VAF is, the better the model represents the actual system. Since the values obtained for the model are close to 100, the model is deemed sufficiently accurate.

What are the limitations of the system? Apart from the problems that were known from the on-set, this thesis has identified another problem which is the inability of the system to control Roll. This has been made apparent in Chapter 6 where a singular value of zero was found in this direction.

Further limitations of the system arise from its workspace, given in Section 6-2-2. Here it is found that the cannot statically reach a surge of more than 0.075m and sway of 0.2m when the Pseudo-Inverse solution is utilized. Note that this is only the case for rotations of zero (excluding roll). When the general tension solution is applied, this increases to 0.25m in surge and 0.275m in sway. The rotations are limited to 1.1 rad in pitch and 0.5 rad in yaw for the pseudo-inverse solution and 1.24 rad in pitch and 0.74 rad in yaw for the general tension solution, again this only holds for translations in the central configuration, i.e $[x \quad y \quad z]^T = [0 \quad 0 \quad 2\text{m}]^T$.

- **How can the limitations be mathematically or numerically analyzed and predicted?** This has effectively been answered above. In the recommendations, another tool for this purpose is suggested called the manipulability, in section 9-4
- **How do these limitations depend on the chosen cable configuration?** This question is not directly answered in the thesis as of yet but is addressed in the recommendations section below, which shows that the limitations of the system depend greatly on the chosen cable configuration. *In fact, a small adjustment in the attachment points of the cables allows for the control of roll. This is shown in Section* **??**.

9-2 Sub-problem answers

In this section the sub-problems that were asked at the introduction of this thesis will be answered. The problem will first be re-iterated and then an answer is provided.

Which control structure can be used? In section 5 a cascaded control structure was proposed where cable forces are controlled in an inner loop and pose is controlled in an outer loop. Such a structure requires the inner loop to be controlled much faster that the outer loop. This structure was largely based on the need for a force controller to ensure positive cables since little to no internal dynamics can be generated. The control structure has proved to perform well in most weather conditions in simulation.

- **How to design and tune this controller?** The controller in this thesis has been designed by first linearizing the model around the central configuration of the workspace. The linear model was then analyzed where it was found that the inputs and outputs that dictate the motion of the and the tension of the cables where completely decoupled in the former case and nearly decoupled in the latter. This allowed the use of SISO design procedures for the controller where loop-shaping has been applied in each of the controllable directions. Finally, the force controller has been slightly adjusted for the hoist cables since the small coupling of these inputs had unexpected effects.

- **How to deal with over-constrained actuation?** The over-constrained actuation is modeled in the Jacobian of the system, making it non-square. Therefore, no normal inverse of the Jacobian exists to obtain a solution the the tensions based on 2-13. This is dealt with by applying the Pseudo-Inverse instead.
- **How to ensure positive cable tensions?** Since the Pseudo-Inverse can yield negative solutions for the tension, a saturation block is implemented of 2N minimum tension such that the force controller will keep tension positive. It was found however that for the worst-case scenario this is not sufficient as negative tension does occur, mostly for hoist cables. This likely relates back to the slight coupling between inputs and outputs that was found for the tension sub-system.

  Furthermore, using the Pseudo-Inverse solution results in a workspace that is smaller than theoretically possible (refer to section 6-2-2). For these reasons, a recommendation is given in section **??** (and Appendix **??**) to apply a more sophisticated Tension Distribution Algorithm of determining the desired cable tensions that make use of the fact that more than one tension distribution can result in a certain configuration by virtually removing up to 3 cables.

Which error margin defines good tracking? From the specification of the real system to be able to lift , the largest allowed error for translations for the scaled system are defined as $\frac{5\text{cm}}{12} = 4\text{mm} = \pm 2\text{mm}$. This value is supported by literature where similar performance has been achieved such as in Lamaury et al. [14]. The error margin for rotation is also obtained from this specification where an angle is obtained based on the 4mm diameter of the smallest and 1m length of the SB to obtain $\sin^{-1}\left(\frac{0.002}{0.5}\right) = \pm 0.004\text{rad}$. This too is supported by literature.

- **For which conditions does the controller still yield good tracking?** Two conditions have been tested. One for calm weather conditions and one for worst-case weather conditions. It was found that the controller performed well within the requirements in the first case, staying within the requirements by a minimum factor of 12.65, i.e. *the maximum RMS error is 12.65 times* ***smaller*** *than the required error.* In the second case the performance fell outside the requirements only for translations, straying outside the requirements by a maximum factor of 4.2882, i.e. *the maximum RMS error is 4.2882 times* ***larger*** *than the required error.* However, the second case did yield short oscillations in the cable tension causing negative tensions. While the system remained stable, this should not occur. It is therefore clear that the controller can perform well for weather conditions close to the worst-case scenario, but that the worst-case itself might cause problems.

  In Appendix **??** the controller is also tested for an operating point that is different from the one it was designed for, namely $[x \quad y \quad z]^T = [0 \quad 0 \quad 4\text{m}]^T$. For the first trajectory the controller performs only slightly worse apart from some initial transients for the roll, while for the second trajectory the system becomes unstable around 40 seconds.
- **How to ensure stability?** This question is not addressed in full in this thesis, but it is found that apart from roll there are no other singularities in the workspace of the . However, the motion sub-system is still *ill-conditioned* as found in section 6-1-1. This

need not be a problem since the reason is a large maximum singular value rather then a small minimum singular value, but could be an indication of instability nonetheless. Results indicate however that the system remains stable during operation.

9-3 Problem statement answer

The specific problem statement can be answered, at least partially, using the information gathered from the answers for the research question, sub-problems and general problem statement:

How to control the end-effector of a redundant CSPM system for offshore application that compensates motions and allows good position tracking for all 6 DOF, seeks to keep cable tensions positive at all times and has a moving actuator frame?

This thesis has outlined the contribution that it makes on the road to answering this question for the *actual* system on-board , i.e. the specific problem. This contribution is two-fold. Firstly, a model in constructed for the test-bed of the system, which is a smaller version of the actual system that is accurately scaled such that it is dynamically similar. The model can be used to quickly test the performance of different controllers because the implementation of controllers on the test-bed can be time-consuming. The second contribution is the design of one such controller that deals with all the problems stated in the problem statement. The controller was found to perform exceptionally well under calm weather conditions and still close to the requirements for worst-case weather conditions. *Since the model is deemed accurate with respect to the test-bed, which in turn is accurate with respect to the actual system, the control strategy given in this thesis is a deemed viable candidate for solving the problem.*

In order to improve the results further however, some recommendations are given. First, recommendations on improving the model are listed such that it can potentially simulate the system even more accurately. Then, recommendations on the controller are given which include the earlier mentioned Tension Distribution Algorithm and implementation of control of roll.

9-4 Model and Analysis recommendations

The modelling process that has been adhered to in this thesis has been a trade-off between accurately capturing the system dynamics whilst simplifying the model for computational efficiency. This has lead to certain concessions, some of which have already been addressed in the thesis. A clear overview of these points and a recommendation for improvement will now be given.

Actuator friction First, and likely having the most influence on the dynamics of the overall system, is the neglecting of the friction in the actuator dynamics. From experiments it is known that the actuators that are used exhibit friction.

One solution, which has been implemented already, is to superimpose a high frequency signal onto the desired torque signals derived in this thesis. This partially gets rid of the stick-slip

portion of the friction. For the viscous- and dry-friction of the actuator, a model could be identified and used as a feed-forward term in the controller. The proper identification for the friction in each of the eight actuators however is a time consuming process and not deemed necessary for the purposes of this thesis. However, for the control of the real system, friction is a non-negligible problem and needs to be dealt with.

inertia In this thesis, the is assumed to be a bar with uniformly distributed mass. In reality, the mass is distributed more unevenly which effects its inertia. A proper identification of the inertia of the can slightly improve the model without decreasing computational efficiency.

Damping identification Although an identification of the cable damping has been carried out for the individual cables, the verification measurements of the system have shown that the parameters do not translate well from cable to system, where the damping is measured to be higher by a factor of six. There are a number of reasons why this could be the case. Firstly, the identification has only been done for the direction parallel to the cable while there is also an orthogonal flexible mode with damping. It is possible that this mode is excited in the actual system. Another possibility is that the coupling between cables adds damping to the entire system.

Thus, the damping identification should ideally be done for the entire system rather than for the individual cables. In other words, the damping could be modeled to act on the , not the cable forces. This requires vastly more measurement data however, for many different points in the workspace, to get a proper function of the damping which is a time-consuming undertaking.

Manipulability For the model analysis, one recommendation would be to analyze what is know as the manipulabilty of the system, defined by Yoshikawa in [31]. The manipulability of a robot is given as both a scalar number, called the *measure of manipulability*, and as a visualization of the force and acceleration capabilities of the end-effector for each configuration of the robot, called the manipulability ellipsoid.

9-5 System and Controller recommendations

This section has been removed for this version of the thesis

Chapter 10

Conclusions and Future work

10-1 Conclusions

In the final chapter of the thesis, a list of conclusions is provided. They are mostly based on the answers given in the discussion, although some conclusions are derived directly from specific sections of the thesis and yet others from the recommendations.

- The derived model of the WF-SB is deemed credible for its purpose of testing controllers that can be applied to the test-bed because it is sufficiently efficient in computation to use for testing purposes and captures the kinematic and dynamic aspects of the system to a satisfactory extent based on a verification with a VAF between 91.4 and 99.9877% in the most excited direction (surge) and a mean VAF of 89.5% between all three translations of the SB motion.
- With the current mechanical design, the roll motion of the SB cannot directly be controller under any circumstances.
- Jacobian singularities are naturally avoided when the cable tensions are kept within their minimum and maximum values at all times.
- The SB *translations* for trajectories under calm weather conditions is shown to stay within the requirements by a minimum factor of 12.65, i.e. the maximum RMS translation error is 12.65 times *smaller* than the required error, meaning that translations are controlled well within their requirements for calm weather conditions
- The SB *rotations* for trajectories under calm weather conditions stay within the requirements by a minimum factor of 259.74, i.e. the maximum RMS rotation error is 259.74 times *smaller* than the required error, meaning that rotations are controlled well within their requirements for calm weather conditions
- The SB *translations* for trajectories under worst-case weather conditions is shown to stray outside the requirements by a maximum factor of 4.2882, i.e. the maximum RMS error is 4.2882 times *larger* than the required error, meaning that translations are controlled slightly outside of their requirements for worst-case conditions.
- The SB *rotations* for trajectories under worst-case weather conditions is shown to stay within the requirements by a minimum factor of 1.0526, i.e. the maximum RMS error is

1.0526 times *smaller* than the required error, meaning that rotations are still controlled within their requirements for worst-case conditions.
- Based on the results, the controller is a viable candidate for solving the specific problem.
- The controller can still yield proper tracking for operating points outside of the one that the controller has been designed for, but the performance decreases and the system can become unstable for certain weather conditions.
- The SB can be fully controlled (in 5DOF) by the use of a minimum of 5 cables since the mechanical design of the system prohibits the control of roll (ϕ) and gravity acts as a sixth cable. Furthermore, the maximum tension in each cable allows for the use of *any* 5 cables to still support the weight of the SB (about 40N) without breaking.
- Choosing the right tension distribution of 5 or more cables for a given pose of the SB, results in an increase of the reachable static workspace using only positive cable tensions. Transitioning between tension distribution solutions during operation can therefore, in principle, also increase the performance of the controller.
- The control of roll can be achieved by slightly changing the mechanical design. This allows to actively control all 6 DOF.

10-2 Future work

Subsequent work can be divided into three categories. The first is with regard to further *research* that can be conducted on the subject. Naturally however, the controller will have to be *verified experimentally* on the test-bed set-up. The control of an offshore crane to compensate motions in 6 degrees-of-freedom in general is beneficial to the safety and efficiency of payload transfer during harsh sea conditions and the contents of this thesis can therefore likely be extended and applied to other applications within offshore.

Future Research

- Research the implementation of the controller for entire workspace.
- Research the performance of the controller when disturbances such as wind are included.
- Research the implementation of a Tension Distribution Algorithm which can potentially increase performance.

Experimental validation

- Implement the controller on the test-bed set-up and verify its performance.
- Determine whether some of the recommendations are required, specifically regarding actuator friction, cable damping and SB inertia.
- Verify that roll can be controlled with the suggested change of cable configuration.

Other applications

- Research the possibility of using this system, or an adaptation of it, for other applications in offshore.

Bibliography

[1] K. Hasselmann, T. P. Barnett, E. Bouws, H. Carlson, D. E. Cartwright, K. Enke, J. A. Ewing, H. Gienapp, D. E. Hasselmann, P. Kruseman, A. Meerburg, P. Müller, D. J. Olbers, K. Richter, W. Sell, and H. Walden, "Measurements of wind-wave growth and swell decay during the Joint North Sea Wave Project (JONSWAP)," *Ergänzungsheft 8-12*, 1973.

[2] D. Stewart, "A Platform with Six Degrees of Freedom," *Proceedings of the Institution of Mechanical Engineers*, vol. 180, pp. 371–386, June 1965.

[3] C. Gosselin, "Cable-driven parallel mechanisms: state of the art and perspectives," *Mechanical Engineering Reviews*, vol. 1, no. 1, pp. DSM0004–DSM0004, 2014.

[4] J. Neupert, T. Mahl, B. Haessig, O. Sawodny, and K. Schneider, "A heave compensation approach for offshore cranes," in *2008 American Control Conference*, pp. 538–543, June 2008.

[5] S. Küchler, T. Mahl, J. Neupert, K. Schneider, and O. Sawodny, "Active Control for an Offshore Crane Using Prediction of the Vessel #x2019;s Motion," *IEEE/ASME Transactions on Mechatronics*, vol. 16, pp. 297–309, Apr. 2011.

[6] N. Xianliang, Z. Jiawen, and X. Jianan, "The heave motion estimation for active heave compensation system in offshore crane," in *2016 IEEE International Conference on Mechatronics and Automation*, pp. 1327–1332, Aug. 2016.

[7] Q. H. Ngo and K.-S. Hong, "Skew control of a quay container crane," *J Mech Sci Technol*, vol. 23, pp. 3332–3339, Dec. 2009.

[8] Q. H. Ngo and K. S. Hong, "Sliding-Mode Antisway Control of an Offshore Container Crane," *IEEE/ASME Transactions on Mechatronics*, vol. 17, pp. 201–209, Apr. 2012.

[9] D.-H. Kim and J.-W. Lee, "Model-based PID control of a crane spreader by four auxiliary cables," *Proceedings of the IMechE*, vol. 220, pp. 1151–1165, Aug. 2006.

[10] P. Gholami, M. M. Aref, and H. D. Taghirad, "On the control of the KNTU CDRPM: A cable driven redundant parallel manipulator," in *2008 IEEE/RSJ International Conference on Intelligent Robots and Systems*, pp. 2404–2409, Sept. 2008.

[11] E. Laroche, R. Chellal, L. Cuvillon, and J. Gangloff, "A Preliminary Study for H_\infty Control of Parallel Cable-Driven Manipulators," in *Cable-Driven Parallel Robots* (T. Bruckmann and A. Pott, eds.), no. 12 in Mechanisms and Machine Science, pp. 353–369, Springer Berlin Heidelberg, 2013.

[12] R. Chellal, L. Cuvillon, and E. Laroche, "A Kinematic Vision-Based Position Control of a 6-DoF Cable-Driven Parallel Robot," in *Cable-Driven Parallel Robots* (A. Pott and T. Bruckmann, eds.), no. 32 in Mechanisms and Machine Science, pp. 213–225, Springer International Publishing, 2015.

[13] J. Lamaury and M. Gouttefarde, "Control of a large redundantly actuated cable-suspended parallel robot," in *2013 IEEE International Conference on Robotics and Automation*, pp. 4659–4664, May 2013.

[14] J. Lamaury, M. Gouttefarde, A. Chemori, and P. Hervé, "Dual-space adaptive control of redundantly actuated cable-driven parallel robots," in *2013 IEEE/RSJ International Conference on Intelligent Robots and Systems*, pp. 4879–4886, Nov. 2013.

[15] S. R. Oh and S. K. Agrawal, "A reference governor-based controller for a cable robot under input constraints," *IEEE Transactions on Control Systems Technology*, vol. 13, pp. 639–645, July 2005.

[16] G. Meunier, B. Boulet, and M. Nahon, "Control of an Overactuated Cable-Driven Parallel Mechanism for a Radio Telescope Application," *IEEE Transactions on Control Systems Technology*, vol. 17, pp. 1043–1054, Sept. 2009.

[17] L.-W. Tsai, "Robot Analysis : The Mechanics of Serial and Parallel Manipulators / L.-W. Tsai.," *ResearchGate*, Jan. 1999.

[18] R. Chellal, E. Laroche, L. Cuvillon, and J. Gangloff, "An Identification Methodology for 6-DoF Cable-Driven Parallel Robots Parameters Application to the INCA 6d Robot," in *Cable-Driven Parallel Robots* (T. Bruckmann and A. Pott, eds.), no. 12 in Mechanisms and Machine Science, pp. 301–317, Springer Berlin Heidelberg, 2013.

[19] B. Zi, B. Y. Duan, J. L. Du, and H. Bao, "Dynamic modeling and active control of a cable-suspended parallel robot," *Mechatronics*, vol. 18, pp. 1–12, Feb. 2008.

[20] I. García-Fernández, M. Pla-Castells, and R. J. Martínez-Durá, "Elevation Cable Modeling for Interactive Simulation of Cranes," in *Proceedings of the 2008 ACM SIGGRAPH/Eurographics Symposium on Computer Animation*, SCA '08, (Aire-la-Ville, Switzerland, Switzerland), pp. 173–181, Eurographics Association, 2008.

[21] P. Miermeister, W. Kraus, T. Lan, and A. Pott, "An Elastic Cable Model for Cable-Driven Parallel Robots Including Hysteresis Effects," in *Cable-Driven Parallel Robots* (A. Pott and T. Bruckmann, eds.), no. 32 in Mechanisms and Machine Science, pp. 17–28, Springer International Publishing, 2015.

[22] "Technocables edition no 6.1 | CarlStahl." Available at: https://www.carlstahl-technocables.com/fileadmin/templates/images/Downloads/Technocables_Edition_6_1_2017.pdf.

[23] S. Skogestad and I. Postlethwaite, *Multivariable Feedback Control: Analysis and Design*. Chichester: Wiley-Interscience, 2 edition ed., Nov. 2005.

[24] A. Berti, J.-P. Merlet, and M. Carricato, "Workspace Analysis of Redundant Cable-Suspended Parallel Robots," in *Cable-Driven Parallel Robots* (A. Pott and T. Bruckmann, eds.), no. 32 in Mechanisms and Machine Science, pp. 41–53, Springer International Publishing, 2015.

[25] M. A. Khosravi and H. D. Taghirad, "Robust PID control of fully-constrained cable driven parallel robots," *Mechatronics*, vol. 24, pp. 87–97, Mar. 2014.

[26] X. Diao, "Singularity analysis of fully-constrained cable-driven parallel robots with seven cables," in *2015 IEEE International Conference on Mechatronics and Automation (ICMA)*, pp. 1537–1541, Aug. 2015.

[27] J. Pusey, A. Fattah, S. Agrawal, and E. Messina, "Design and workspace analysis of a 6–6 cable-suspended parallel robot," *Mechanism and Machine Theory*, vol. 39, pp. 761–778, July 2004.

[28] R. G. Regis, "On the properties of positive spanning sets and positive bases," *Optim Eng*, vol. 17, pp. 229–262, Mar. 2016.

[29] X. Diao, "Singularity analysis of fully-constrained cable-driven parallel robots with seven cables," in *2015 IEEE International Conference on Mechatronics and Automation (ICMA)*, pp. 1537–1541, Aug. 2015.

[30] M. Arsenault, "Workspace and stiffness analysis of a three-degree-of-freedom spatial cable-suspended parallel mechanism while considering cable mass," *Mechanism and Machine Theory*, vol. 66, pp. 1–13, Aug. 2013.

[31] T. Yoshikawa, "Manipulability of Robotic Mechanisms," *The International Journal of Robotics Research*, vol. 4, pp. 3–9, June 1985.

Glossary

List of Symbols

Abbreviations

$()^{\dagger}$	Moore-Penrose Pseudo-Inverse
$\boldsymbol{\lambda}$	Vector to scale $\mathbf{N}$
$\boldsymbol{\tau}$	Vector of motor torques
ϵ	Cable elongation
γ	Condition number for controllability of MIMO systems
Λ	Relative Gain Array matrix
ω	Angular velocity
ϕ, θ, ψ	Roll angle, Pitch angle, Yaw angle in Euler convention
$\mathbf{a}_i$	Vector from base frame origin to i^{th} attachment point in the same frame
$\mathbf{A}_k$	State-space A matrix
$\mathbf{B}$	Cable damping diagonal matrix
$\mathbf{b}_i$	Vector from moving platform frame origin to i^{th} attachment point in the same frame
$\mathbf{B}_k$	State-space B matrix
$\mathbf{c}(\dot{\mathbf{q}}, \mathbf{q})$	Vector containing Coriolis and Centrifugal forces
$\mathbf{C}_k$	State-space C matrix
$\mathbf{D}_k$	State-space D matrix
$\mathbf{f}$	Vector of SB forces
$\mathbf{G}$	system gain matrix
$\mathbf{g}(\mathbf{x})$	Gravity vector
$\mathbf{I}$	Inertia matrix
$\mathbf{J}$	Jacobian matrix
$\mathbf{J}_B$	Basis for Jacobian
$\mathbf{J}_\omega$	Mapping between Euler angle derivatives and angular velocities
$\mathbf{K}$	Cable stiffness diagonal matrix

$\mathbf{L}$	Stretched cable length diagonal matrix
$\mathbf{l}$	JS coordinates of cable lengths
$\mathbf{L}_0$	Unstretched cable length diagonal matrix
$\mathbf{l}_0$	Vector of un-stretched cable lengths
$\mathbf{l}_d$	Cable length static offsets
$\mathbf{l}_i$	Vector of i^{th} link/cable length
$\mathbf{m}$	Vector of SB moments
$\mathbf{M}(\mathbf{x})$	Mass matrix
$\mathbf{N}$	Null-space of transposed Jacobian
$\mathbf{N}_d$	Diagonal matrix of gear-ratio n for first 2 entries and 1 for the other entries
$\mathbf{o}_{sb}$	Orientation coordinates of the SB
$\mathbf{o}_{wf}$	Orientation coordinates of the WF
$\mathbf{p}_{ai}$	Vector between reference frame and WF i^{th} attachment point
$\mathbf{p}_{bi}$	Vector between reference frame and SB i^{th} attachment point
$\mathbf{p}_{sb}$	Cartesian coordinates of the SB
$\mathbf{p}_{wf}$	Cartesian coordinates of the WF
$\mathbf{q}$	Vector of motor angles
$\mathbf{R}_B^A$	Rotation matrix between WF-frame (A) and SB-frame (B)
$\mathbf{R}_B^r$	Rotation matrix between WF-frame (A) and SB-frame (B)
$\mathbf{R}_B^r$	Rotation matrix between reference frame (r) and SB-frame (B)
$\mathbf{R}_w$	Matrix of motor radii
$\mathbf{t}$	Vector of cable tensions
$\mathbf{U}$	Unitary matrix of output singular vectors
$\mathbf{u}$	State-space input vector
$\mathbf{u}_i$	unit vector (direction) of i^{th} link/cable
$\mathbf{w}$	Vector of SB wrench
$\mathbf{x}_i$	State variable
$\mathbf{x}_{sb}$	TS coordinates of SB pose
$\mathbf{x}_{wf}$	TS coordinates of WF pose
$\mathbf{y}$	State-space output vector
A_0	Cable cross-sectional area
C_f	Force Controller
C_m	Motion Controller
g	Gravitational constant
K_d	Derivative control gain
K_i	Integrative control gain
K_p	Proportional control gain
l_i	Stretched length of i^{th} link/cable
$l_{0,i}$	un-stretched length of i^{th} link/cable
m	Mass

Q^{ncons}	Non-conservative forces acting on the SB
T	Kinetic energy
t_i	i^{th} cable tension
t_s	Settling time
T_d	Frequency corresponding to derivative action in a controller
T_i	Frequency corresponding to integral action in a controller
V	Potential energy
$\mathbf{\Sigma}$	Diagonal matrix of descending singular values
κ	Condition variable for Jacobian
$\mathbf{V}$	Unitary matrix of input singular vectors
b	Cable damping
E	Young's modulus
k	Cable stiffness
n	Gear ratio
r	Winch radius
s	Laplace complex variable
t	time

List of Acronyms

CDPM	Cable-Driven Parallel Mechanism
CSPM	Cable-Suspended Parallel Mechanism
FK	Forward Kinematics
HIL	Hardware In the Loop
IK	Inverse Kinematics
JS	Joint-space
TS	Task-Space
TD	Tension Distribution
MC	Motion Controller
FC	Force Controller
BW	Band-Width
GM	Gain Margin
PM	Phase Margin
WS	Workspace

SVD	Singular Value Decomposition
RGA	Relative Gain Array
PID	Proportional-Integral-Derivative
PI	Proportional-Integral
RMS	Root Mean Square
DOF	Degrees Of Freedom
MIMO	Multiple Input Multiple Output
SISO	Single Input Single Output
VAF	Variance Accounted For